
# BRNO UNIVERSITY OF TECHNOLOGY

VYSOKÉ UČENÍ TECHNICKÉ V BRNĚ

## FACULTY OF ELECTRICAL ENGINEERING AND COMMUNICATION

FAKULTA ELEKTROTECHNIKY
A KOMUNIKAČNÍCH TECHNOLOGIÍ

## DEPARTMENT OF BIOMEDICAL ENGINEERING

ÚSTAV BIOMEDICÍNSKÉHO INŽENÝRSTVÍ


# DATA ANALYSIS FOR QUANTITATIVE MR RELAXOMETRY

ANALÝZA DAT PRO KVANTITATIVNÍ MR RELAXOMETRII

BACHELOR'S THESIS
BAKALÁŘSKÁ PRÁCE


AUTHOR
AUTOR PRÁCE

Hana Páralová

SUPERVISOR
VEDOUCÍ PRÁCE

Ing. Martin Mézl, Ph.D.



BRNO 2022

BRNO UNIVERSITY OF TECHNOLOGY
FACULTY OF ELECTRICAL ENGINEERING AND COMMUNICATION

# Bachelor's Thesis

Bachelor's study program **Biomedical Technology and Bioinformatics**

Department of Biomedical Engineering

***Student:*** Hana Páralová ***ID:*** 222536

***Year of study:*** 3 ***Academic year:*** 2021/22

**TITLE OF THESIS:**

## Data analysis for quantitative MR relaxometry

**INSTRUCTION:**

1) Get acquainted with the principles of contrast formation in MR images and their use for quantitative imaging of relaxation times T1 and T2 or T2*. Characterize typical experimental methods based on steady state and data analysis methods leading to the estimation of relaxation parameters and their errors. 2) Using existing functions for loading original data in Bruker formats, existing display functions and optimization functions, implement in Python the calculation of relaxation parameters and estimates of their accuracy for selected types of experiments. 3) Assess the quality of the models with the data obtained from phantom measurements, evaluate the reproducibility, accuracy and precision of the estimates, compare the theoretical estimates of variances with the experimentally obtained ones, analyze the problems found. 4) Suggest such modifications to the models or measurements that could lead to an improvement of the quality of relaxation parameter estimation. 5) Verify the most important results resulting from phantom measurements on mouse or rat brain relaxometry on the Bruker Biospec 9.4 T scanner at ÚPT AV ČR, v. v. i.

**RECOMMENDED LITERATURE:**

1. Bernstein MA, King KF, Zhou XJ: Handbook of MRI pulse sequences. Elsevier Academic Press 2004, ISBN-13: 978- 0-12-092861-3

2. Granziera C, Wuerfel J, Barkhof F, et al: Quantitative magnetic resonance imaging towards clinical application in multiple sclerosis. Brain, vol. 144, issue 5, pg. 1296-1311, 2021. doi: 10.1093/brain/awab029

***Date of project specification:*** 7.2.2022 ***Deadline for submission:*** 27.5.2022

***Supervisor:*** Ing. Martin Mézl, Ph.D.

**doc. Ing. Jana Kolářová, Ph.D.**
Chair of study program board

## ABSTRACT

This work deals with the implementation of an algorithm for data analysis for quantitative magnetic resonance relaxometry. Magnetic resonance (MR) is a non-invasive imaging technique using the magnetic properties of atomic nuclei. The motivation for the use of relaxation parameters of tissue is scanner-independent diagnostics. The work describes the essential theoretical foundations of MR mechanisms and the contrast mechanisms. Using them, an algorithm in Python is designed for fitting the relaxation parameters of the sample. Fitting is done according to an exponential model functions for three different combinations of parameters - individual fitting of T1 or T2 relaxation time and simultaneous fitting of both times. A locally linearized model and Cramer-Rao lower bounds are used to calculate the standard deviation of the fitted parameters. The results of the work were successfully verified on a fixed rat brain relaxometry.

## KEYWORDS

Magnetic resonance, magnetic resonance imaging, quantitative relaxometry, data analysis, programming in Python, parameter fitting, standard deviation estimation, locally linearized model, Cramér-Rao lower bounds

## ABSTRAKT

Tato práce se zabývá implementací algoritmu pro analýzu dat pro kvantitativní relaxometrii magnetické rezonance. Magnetická rezonance (MR) je neinvazivní zobrazovací technika využívající magnetických vlastností atomových jader. Motivací pro využívání relaxačních parametrů tkání je nezávislost na MR skenerech či jednotlivých pacientech. V práci jsou popsány nezbytné teoretické základy MR mechanizmů a vzniku kontrastu v obrazech. S jejich využitím je navržen algoritmus v jazyce Python pro fitování relaxačních parametrů vzorku. Fitování probíhá podle exponenciálních modelových funkcí pro tři různé kombinace parametrů - individuální fitování T1 nebo T2 relaxačního času a simultánní fitování obou časů. Pro výpočet směrodatné odchylky fitovaných parametrů je použit lokálně linearizovaný model a dolní meze podle teorie Cramér-Rao. Výsledky práce byly úspěšně ověřeny na relaxometrii fixovaného potkaního mozku.

## KLÍČOVÁ SLOVA

Magnetická rezonance, kvantitativní relaxometrie, analýza dat, programování v jazyce Python, fitování parametrů, odhad směrodatné odchylky, lokálně linearizovaný model, Cramér-Rao dolní meze

# ROZŠÍŘENÝ ABSTRAKT

Tato bakalářská práce se zabývá implementací algoritmu pro analýzu dat pro kvantitativní relaxometrii magnetické rezonance. Magnetická rezonance (MR) je neinvazivní zobrazovací technika využívající magnetických vlastností atomových jader, zejména jader vodíkových. Zkoumaný objekt je vložen do homogenního magnetického pole, které je generováno skenerem. Intenzita pole je v jednotkách Tesla. Budicí radiofrekvenční (RF) cívky na vhodné frekvenci pak generují signál, který excituje rezonující jádra. Magnetický vektor se po skončení RF pulzu navrací zpět do rovnovážného stavu pomocí relaxačních mechanizmů. Emise elektromagnetického vlnění je snímána a jako měřený signál využita pro zobrazování relaxačních parametrů zkoumaného objektu.

Motivací pro využívání MR relaxometrie je hlavně bezpečnost vyšetření, při kterém není použito ionizační záření. Možnými kontraindikacemi k vyšetření mohou být MR nekompatibilní kovy v těle pacienta jako například kardiostimulátor nebo různé kostní výztuhy a implantáty. Dále je výhodou dobrý kontrast pro měkké tkáně, objektivní porovnání relaxometrie těchto tkání a rozpoznávání a identifikace patofyziologií v organizmu, hlavně nádorů. MR relaxometrie se využívá ve výzkumu léčiv k určení místa jejich působení pomocí značení kontrastními látkami.

První kapitola práce se věnuje nezbytným teoretickým základům pro popis jevu magnetické rezonance, nukleární magnetické rezonance a mechanizmům vzniku kontrastu v obrazech. Jsou zde vysvětleny základní pojmy jako jaderný spin, magnetické pole a magnetizace. Pro pochopení principu fungování MR mechanizmů jsou zde vysvětleny pojmy jako Larmorova precese, volně indukovaný signál (free induction decay, FID) a gradientní magnetické pole, které je nezbytné pro excitaci dané oblasti. Dále jsou popsány relaxační mechanizmy reprezentované především relaxačními časy T1 a T2. Ty jsou definovány jako spin-mřížková (T1, neboli návrat vektoru magnetizace do rovnovážného směru) a spin-spinová (T2, neboli ztráta fázové koherence dipólů) relaxace.

Ve druhé kapitole je zmíněna historie měření od měření relaxace ve spektroskopii až po nejmodernější metody deep learningu a fingerprintingu. V této kapitole jsou popsány základní pulzní sekvence jako je gradientní echo, spinové echo a inversion recovery, a z nich odvozené pulzní sekvence.

Třetí kapitola diskutuje o důvodech pro použití relaxometrie. Těmi jsou především nezávislost měřených parametrů na skeneru nebo instituci, tím je dosaženo možnosti porovnávání relaxačních parametrů nezávisle na pacientovi či nastavení parametrů snímání. Lepší kontrast pro rozlišení jednotlivých tkání díky zobrazování relaxačních map. Určující role při rozpoznávání patofyziologií díky porovnání měřených relaxačních parametrů. A v neposlední řadě sledování koncentrace kontrastních látek v organizmu a jejich trajektorií. Konkrétně v této prácí bylo použito

nanolipozomů značených gadoliniem (ovlivňuje relaxační parametry molekul vody v okolí), které se využívají ke značenému transportu léčiv mimo krevní oběh skrz hematoencefalickou bariéru do mozku.

Kapitola čtvrtá popisuje použité metody pro vznik algoritmu, jeho samotnou implementaci a odhad chyby. Dále je zde popsáno rozložení a obsah fantomů, na kterých byly provedeny testy funkčnosti a správnosti algoritmu.

V páté kapitole jsou diskutovány výsledky.

Algoritmus byl vyvíjen v programovacím prostředí jazyka Python. Měření probíhalo na preklinickém MR systému Bruker Biospec 9.4 T scanner na Ústavu přístrojové techniky Akademie věd ČR, v. v. i.

K ověření správnosti fitovacích modelů byly vytvořeny pokusné vzorky - fantomy tak, aby bylo možné prozkoumat relaxační parametry. Pravdivost modelů byla dále ověřena na relaxometrii myšího mozku.

V rámci implementace samotného algoritmu byly použity pythonovské knihovny `numpy`, `scipy` a `matplotlib` a také knihovna pro načítání brukerovských dat vytvořená na ÚPT AV. Po načtení knihoven jsou načtena měřená data ve formě datasetu se všemi parametry měření, ty jsou poté využity při fitování. Byly vytvořeny tři pythonovské skripty pro tři použité fitovací metody - individuální T1 fitování, individuální T2 fitování a simultánní fitování obou relaxačních parametrů. Pro každou metodu existuje jiná modelová funkce.

Data pro fitování byla vybírána na základě hodnot v pixelu převyšujících odhadnutou hodnotu šumu v obraze. Hodnota šumu byla počítána z okrajových pixelů obrazu za předpokladu, že se zde nenachází fantom nebo duch. Tato skutečnost může být uživatelem vizuálně ověřena při spuštění programu.

Fitování parametrů poté probíhalo pomocí minimalizační funkce `least.squares` z knihovny `scipy.optimize`. Fitované parametry byly zapsány do matice, ze které byla následně vypočítáná směrodatná odchylka fitovaných parametrů. Výpočet směrodatné odchylky byl proveden dvěma způsoby - lokálně linearizovaným modelem a výpočtem dolních mezí metodou Cramér-Rao. Všechny fitované parametry a jejich vypočtené směrodatné odchylky jsou nakonec zobrazeny v šedotónových obrázcích s přiloženou škálou hodnot.

Správnost a funkčnost programu byla testována na datech měřených na fantomovém vzorku, který obsahoval gadoliniem značené nanolipozomy. Tyto výsledky byly dále úspěšně ověřeny na relaxometrii fixovaného potkaního mozku.

PÁRALOVÁ, Hana. *Data analysis for quantitative MR relaxometry*. Brno: Brno University of Technology, Faculty of Electrical Engineering and Communication, Department of Biomedical Engineering, 2022, 65 p. Bachelor's Thesis. Advised by Ing. Martin Mézl, Ph.D.

# Author's Declaration

| | |
|---|---|
| **Author:** | Hana Páralová |
| **Author's ID:** | 222536 |
| **Paper type:** | Bachelor's Thesis |
| **Academic year:** | 2021/22 |
| **Topic:** | Data analysis for quantitative MR relaxometry |

I declare that I have written this paper independently, under the guidance of the advisor and using exclusively the technical references and other sources of information cited in the paper and listed in the comprehensive bibliography at the end of the paper.

As the author, I furthermore declare that, with respect to the creation of this paper, I have not infringed any copyright or violated anyone's personal and/or ownership rights. In this context, I am fully aware of the consequences of breaking Regulation § 11 of the Copyright Act No. 121/2000 Coll. of the Czech Republic, as amended, and of any breach of rights related to intellectual property or introduced within amendments to relevant Acts such as the Intellectual Property Act or the Criminal Code, Act No. 40/2009 Coll. of the Czech Republic, Section 2, Head VI, Part 4.

Brno ..... .....

author's signature*

*The author signs only in the printed version.

# ACKNOWLEDGEMENT

I would like to thank my advisor Ing. Martin Mézl, Ph.D. for his valuable advices and smooth communication. Furthermore, I would like to thank to my external supervisor Ing. Zenon Starčuk, CSc. for all his time, advices, patience during explaining necessary knowledge and willingness to help me with troubleshooting. And last, but not least to my family and friends for all their support.

# Contents

# List of Figures

# Introduction

This work focuses on quantitative MR relaxometry parameters fitting, particularly T1 and T2 relaxation times. MR relaxometry has become an important tool in quantitative MRI by providing maps which interpret the individual contrast mechanisms independent of the MR protocol (software) or the MR hardware. Unlike conventional qualitative MR images, the quantitative images can provide the absolute interpretation of signal intensity in tissues. Then the comparison of images from different scanners or institutions can be objective thanks to quantitative measurement of fundamental parameters such as relaxation times.

The general description of basic theory of magnetic resonance (MR) is the topic of the first chapter, including nuclear magnetic resonance (NMR) and magnetic resonance imaging (MRI) and contrast mechanisms. Chapter 2 focuses on the history of relaxation measurement from relaxation in spectroscopy, through MRI pulse sequences, up to state-of-the-art techniques using replacing regularity by pseudo-randomness such as fingerprinting or deep learning.

Chapter 3 discusses the main motives for relaxometry, including scanner independent diagnostics and interinstitutionally transferrable knowledge, optimizing MRI pulse sequences for obtaining specific contrast for discrimination of tissues, obtaining intermediary parameters reflecting contrast agent concentration and securing physical information underpinning pathophysiology research.

Materials and methods used in this work are introduced in chapter 4. These include MRI experiment settings, fitting methods, algorithm implementation and confidence interval estimation. Results are presented in chapter 5.

# 1 Nuclear magnetic resonance

## 1.1 Spin, magnetic field and magnetization

In the human body 62% of all atoms are hydrogen atoms. Their nuclei have a spin of ½, which is manifested by magnetic moment and angular momentum. Their behavior could be compared to that of a tiny cylindrical bar magnet rotating about its axis: it has similar magnetic and inertial properties. These qualities determine the behavior of these nuclei in an external magnetic field, where they tend to partially align along this external magnetic field. Thanks to the excess of nuclei with the lower-energy orientation, the result is a macroscopic magnetic moment. Its amount results from the equilibrium distribution of orientations, and can be calculated from the Boltzmann distribution of spin energies. The magnetization is then the sum of magnetic moments per unit volume.

The main magnetic field in a MRI scanner is a strong, static field, $B_0$, generated by the MRI scanner magnet (usually superconducting, or permanent). It is measured in SI units of Tesla [T] or CGS units of Gauss [G]. In addition, another magnetic field, $B_1$, perpendicular to $B_0$, is generated by the MRI scanner in the form of radiofrequency (RF) pulses with a short duration serving to rotating (exciting, refocusing, or deexciting) the spins. Another set of magnetic fields generated by the MRI scanner on demand are the 3 gradient fields which can modify the static field $B_0$ linearly along any spatial direction. [18]

The MRI signal is obtained from the nuclear magnetization component perpendicular to the static field. It is proportional to the proton density linearly, but it is also affected by other parameters such as the relaxation properties and the type and parameters of the excitation pulse sequence. Depending on the pulse sequence, the MRI images reflect the concentrations of water, fat, and other compounds by signals specifically reflecting the properties of hydrogen nuclei.

## 1.2 Precession

The static magnetization is stationary in the $B_0$ field. After a short $B_1$ pulse is applied, the magnetization is tilted from its equilibrium ($B_0$ orientation), and the resulting magnetization starts precessing around $B_0$. This phenomenon is called Larmor precession. The precessing magnetization produces an oscillating transverse field (perpendicular to $B_0$), thanks to which in the receive coil, immediately the signal induction begins. Simultaneously with the total magnetization vector being rotated away from the equilibrium, the magnetization undergoes relaxation back

to the equilibrium. Typically, the relaxation processes are much slowlier than the oscillation due to precession (e.g. 10-5000 ms versus 2-40 ns).

The magnetization vector rotates about the main magnetic field with an angular velocity, $\omega_0$, where

$$\omega_0 = 2\pi f_0 \tag{1.1}$$

and $f_0$ is known as the Larmor frequency, given by

$$f_0 = \gamma B_0 \tag{1.2}$$

where $B_0$ is the applied main magnetic field and $\gamma$ is the gyromagnetic ratio (in Hz/T), which for protons equals to approximately $42,6 \cdot 10^6$ Hz/T. For the B1 excitation to be successful, it has to spectrally overlap the Larmor frequency so that resonance transfer of energy can occur, and for the sake of efficiency, on-resonance RF pulses whose carrier is close to the Larmor frequency are used.

## 1.3 Free induction decay (FID)

Right after the excitation by a hard (i.e. very short, broadband) or soft (i.e. usually 1-20 ms long, band-limited) RF pulse, the nuclear spins are tilted towards the transverse plane with the same phase, adding up to the maximum-coherence signal. The tilted magnetization performs precession motion. Immediately, the initially coherent spins dephase due to random interactions of any kind spins, such as with magnetic field inhomogeneities or dipolar interactions [1], and the original coherence is getting lost. This transversal coherence loss is partially reversible (local static field inhomogeneity) and partially irreversible (given by random interactions between excited hydrogen atoms with surroundings, or each other).

Simultaneously the spins realign in the direction of $B_0$ and return to the Boltzman equilibrium exponentially with a time constant $T1$ (longer than $T2$, varies with tissues).

## 1.4 Gradient field, excitation of a selected slice

The gradient fields are referred to as $B_x$, $B_y$, $B_z$ and the magnetic field in MRI scanner is given by

$$B = B_0 + B_x + B_y + B_z. \tag{1.3}$$

These gradients are applied multiple times during the experiment and are used for slice selection, image encoding (including frequency and phase encoding), diffusion weighting, or spurious signal suppression.

To excite a specific slice perpendicular to $z$ direction, the gradient in $z$ direction is applied and the required slice-center Larmor frequency is calculated and set as the carrier frequency for the excitation. The carrying frequency is amplitude- (and sometimes also phase-) modulated so that the excitation affects the required frequency bandwidth. In small-flip-angle approximation, the frequency spectrum of the excitation pulse corresponds to the distribution of the flip angle. Thus if we need a slice selection profile with a constant flip angle within, and a zero flip angle outside this region, we modulate the carrier amplitude by sinc (sin t/t). [18]

Once the desired slice is excited, the spin positions inside the excited slice are encoded by gradients applied in the $x$-$y$ plane (still assuming that the $z$ direction is perpendicular to the excited slice). Then the magnetization in the selected area is characterized by phase

$$\theta(t) = 2\pi(k_x(t)x + k_y(t)y) \tag{1.4}$$

where

$$k_x(t) = \gamma \int G_x(\tau)d\tau, 0, t, \tag{1.5}$$

$$k_y(t) = \gamma \int G_y(\tau)d\tau, 0, t, \tag{1.6}$$

and $G_x$ and $G_y$ represent the gradients waveforms.

The resulting signal measured in the receiver coil is the signal from all spins expressed as

$$s(t) = \int f(x,y)e^{i2\pi(k_x x + k_y y)}dxdy \tag{1.7}$$

where $f(x,y)$ describes the distribution of magnetization in the moment when $k_x$=$k_y$=0. This equation expresses the fact that the signal at time $t$ corresponds to the value of the Fourier transform $F(k_x, k_y)$ of $f(x,y)$ in the spatial-frequency point $(k_x(t), k_y(t))$, i.e.,

$$s(t) = F(k_x(t), k_y(t)). \tag{1.8}$$

[18]

## 1.5 T1 and T2 relaxation times

Relaxation is in fact a process related to molecular motion which causes random interactions and energy exchange.

$T1$ relaxation time, also known as the spin-lattice relaxation time, is the recovery time of longitudinal magnetization (in the same direction as the static magnetic field). $T1$ involves energy exchange between protons and the lattice (surrounding macromolecules, lipids, and proteins). The sequence can be designed in such a way

that the resulting images are predominantly $T1$ weighted; in this case the contrast between tissues is given by the various recovery rates of longitudinal magnetization. $T1$ can be modified by Gd-based contrast agents.

$T2$ relaxation is the time describing the loss of phase coherence (or entropy increase) of the water protons due to irreversible interactions and spin exchange between them. $T2$ is termed the spin-spin relaxation. $T2$ can be shortened by iron-oxide-based contrast agents.

$T2*$ (also called apparent $T2$) is related to the spin-spin relaxation time $T2$ by

$$\frac{1}{T2*} = \frac{1}{T2} + \frac{1}{T2'} \tag{1.9}$$

where

$$T2' \sim \frac{1}{\gamma \Delta\beta} \tag{1.10}$$

where $\Delta\beta$ is the $B_0$ field inhomogeneity (standard deviation) and $T2'$ is termed microscopic dephasing and refers to static inhomogeneities caused by dephasing of the water protons due to small variations in their local magnetic fields.

Tab. 1.1: Typical values of relaxation times for different tissues at 1.5T.

| Tissue | T1 [s] | T2 [ms] |
|---|---|---|
| Water/CSF | 4 | 2000 |
| Fat | 0.25 | 70 |
| Gray matter | 0.9 | 90 |
| Muscle | 0.9 | 50 |
| Liver | 0.5 | 40 |

## 1.6 Magnetic resonance imaging and contrast mechanisms

To generate an image, the surveyed volume of tissue must be spatially encoded to define a position in a slice and allocate the signal intensities in the plane. The displayed image is then composed of a set of pixels or voxels. Let's consider a single slice already excited.

The k-space sampling can be done by a rectilinear or a nonrectilinear trajectory, such as spiral or projection acquisition. MR image reconstruction simply requires 2D- or 3D-IFT, which can be calculated by a series of FFTs. These can be applied

only at rectilinearly sampled data. Consequentially, the data sampled using nonrectilinear trajectories require regridding - an operation resampling data to a rectilinear grid - to enable the usage of FFTs. Projection data can also be reconstructed using filtered back-projection, typical for CT. [2]

Another difference in sampling can be the k-space coverage. When the data are sampled symmetrically over both positive and negative spatial frequencies, we call this the full Fourier acquisition. In the partial Fourier acquisition the k-space sampling is not symmetric: typically, one half of k-space is fully filled and the other half contains only a small amount of data. This approach can considerably shorten the scan time due to reduced acquisition time if the properties of excitation allow the use of some symmetries in k-space data. [2]

# 2 History of relaxation measurement

## 2.1 Relaxation in spectroscopy

In NMR spectroscopy, the spectrum can be calculated quite precisely using classical electromagnetic theory. Each sample either absorbs, or emits electromagnetic energy of a certain wavelength $\lambda$, which can be measured. Then a spectrum is expressed by the distribution and intensities of the measured energy. Therefore, the MR spectroscopy is providing information about the physical and chemical properties of the sample.

The fundamentals of MR spectroscopy and MR imaging are the same. Both are built on the basic physics discovered by Bloch et al. The signals acquired from MR measurement can be displayed either as converted signal intensities to gray scale image or as a function of frequency as a spectral plot. [10]

### The Bloch equations

In 1946 the differential equations to model the dynamics of the magnetization produced by magnetic dipoles in magnetic field were derived by Felix Bloch, who won the Nobel prize in Physics in 1952 for his discovery. In the equations, the precession and exponential relaxation (described by $T1$ and $T2$) are included. The equations are written separately for the three components of magnetization $M_x$, $M_y$ and $M_z$. [25]

To describe the Bloch equations [3] we need to decompose the vector of magnetization $\mathbf{M}$ into longitudinal (parallel to $B_0$), represented by a real value $M_z$, and transverse (perpendicular to $B_0$, represented by a complex value $M_- = M_x + iM_y$ and $M_+ = M_x - iM_y$. Then the magnetic moment $M$ per unit volume is given by

$$\frac{d\mathbf{M}}{dt} = \mathbf{M} \times \gamma\mathbf{B}. \tag{2.1}$$

Bloch equations without relaxation

$$\frac{d\mathbf{M}}{dt} = \mathbf{M}(t) \times \gamma\mathbf{B}(t) \tag{2.2}$$

$$\frac{d}{dt}\begin{pmatrix} M_x \\ M_y \\ M_z \end{pmatrix} = \begin{pmatrix} 0 & \gamma B_z(t) & -\gamma B_y(t) \\ -\gamma B_z(t) & 0 & \gamma B_x(t) \\ \gamma B_y(t) & -\gamma B_x(t) & 0 \end{pmatrix}\begin{pmatrix} M_x \\ M_y \\ M_z \end{pmatrix} \tag{2.3}$$

Bloch equations with relaxation

$$\frac{d}{dt}\begin{pmatrix} M_x \\ M_y \\ M_z \end{pmatrix} = \begin{pmatrix} -1/T2 & \gamma B_z(t) & -\gamma B_y(t) \\ -\gamma B_z(t) & -1/T2 & \gamma B_x(t) \\ \gamma B_y(t) & -\gamma B_x(t) & -1/T1 \end{pmatrix} \begin{pmatrix} M_x \\ M_y \\ M_z \end{pmatrix} + \frac{1}{T1}\begin{pmatrix} 0 \\ 0 \\ M_\infty \end{pmatrix} \tag{2.4}$$

where $T1$ relaxation is the restoration of equilibrium $M_\infty$ and $T2$ relaxation is the decay of $M_x$, $M_y$.

## 2.2 MRI pulse sequences

### Basic pulse sequences

1. **Gradient echo pulse sequence**
   Gradient echo pulse sequence (GRE) is using the free induction decay (FID) for imaging. 3 parameters are used - the repetition time $TR$, , the echo time $TE$ and the flip angle $\alpha$. The signal intensity of GRE depends on parameters of the sequence $TR$, $TE$, $\alpha$, the tissue parameter proton density $S_0$ and the relaxation times $T1$ and $T2$. [4] In addition to fast acquisition, GRE pulse sequence can provide images with bright blood signal. The GRE images are contrast weighted by $e^{-TE/T2*}$ what makes them more prone to signal loss due to $T2*$ instead of $T2$. [2]

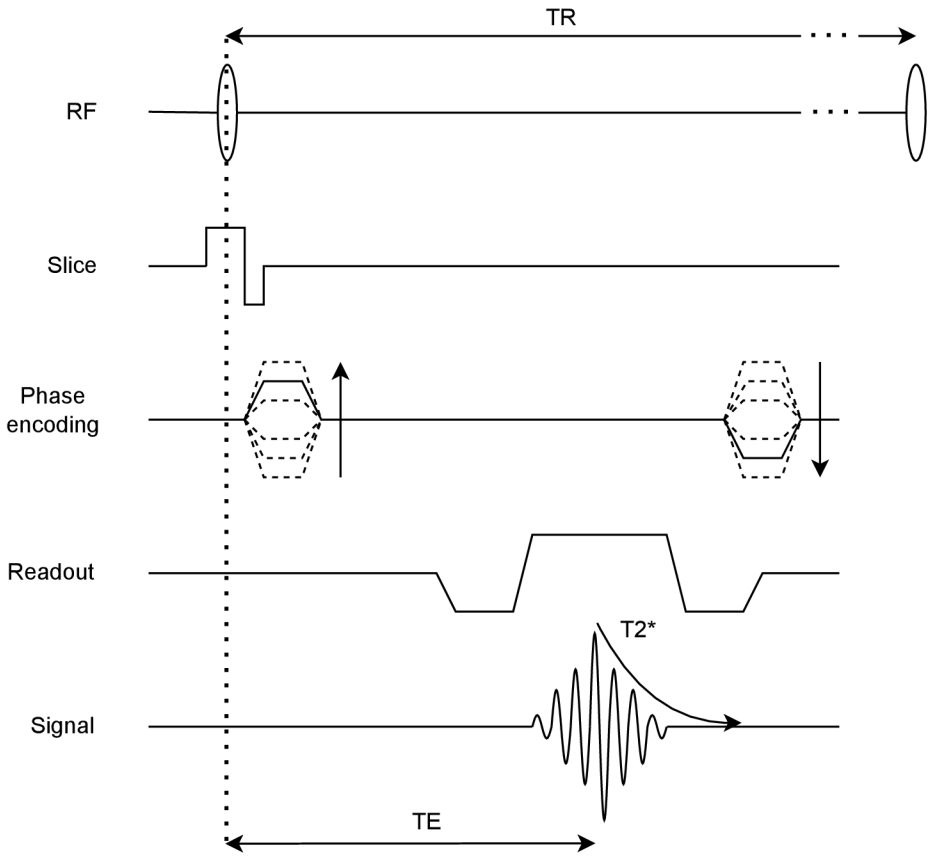


Fig. 2.1: Gradient echo pulse sequence diagram.

2. **Spin echo pulse sequence** After the initial 90° RF pulse is applied, the individual magnetization vectors are tilted and start dephasing due to magnetic field inhomogeneities and dipolar interactions. This dephasing can be reversed through subsequent application of a 180° RF pulse. These vectors are rotated in the transverse plane. This causes the conversion of the transverse magnetization phase $\phi$ into a negative phase $-\phi$. After this rotation, all vectors precess at the same rate as before. At $TE$ they all rephase and create an echo. That's why the 180° pulse is usually called the refocusing pulse. [4]

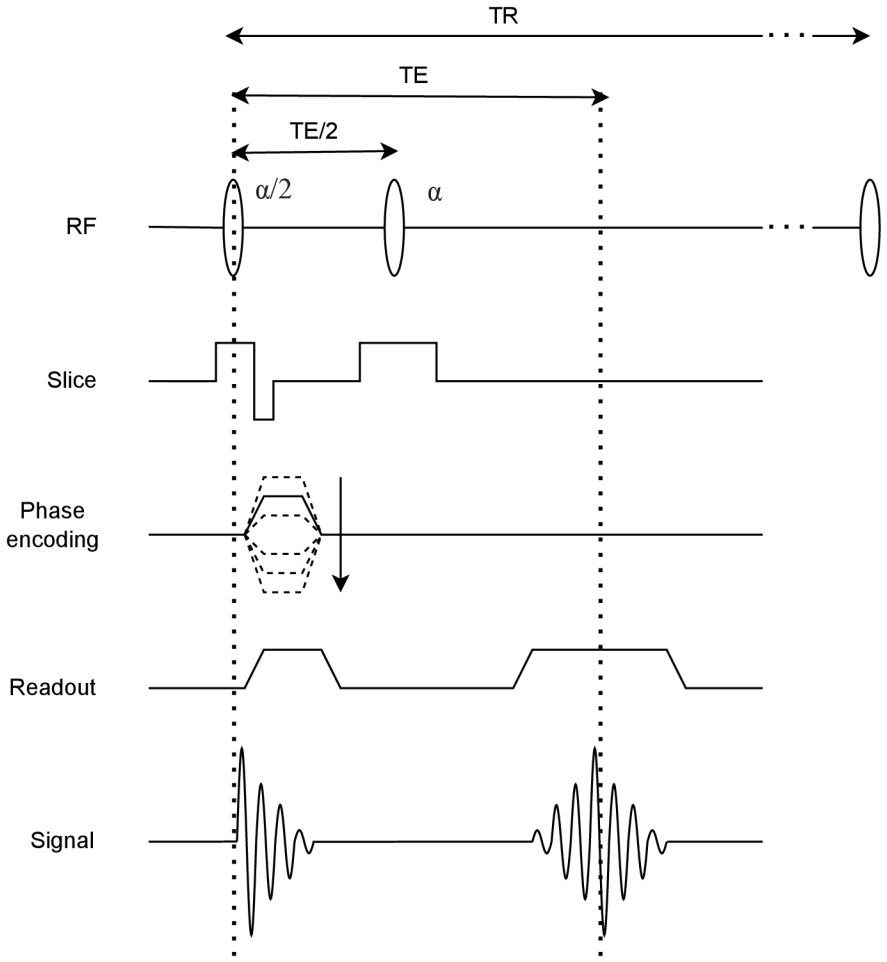


Fig. 2.2: Spin echo pulse sequence diagram.

3. **Inversion recovery pulse sequence**
   Inversion recovery (IR) is a useful magnetization preparation module used before other imaging pulse sequences in order to enhance $T1$ weighting of signal intensities. IR begins with a 180° inversion pulse, which inverts the longitudinal magnetization from $+z$ to $-z$ direction. After a delay TI (inversion time), a host pulse sequence such as GRE or SE is started. The resulting signal reflects the degree of recovery during TI. When TI is comparable to $T1$, the image is strongly $T1$-weighted, even more pronounced than a typical $T1$-weighted image because of wider dynamic recovery range (from $-M_0$ to $M_0$ instead of from 0 to $M_0$). [4]


Fig. 2.3: Inversion recovery pulse sequence diagram.

## GRE derived pulse sequences

When the transverse magnetization is actively suppressed to zero before each excitation pulse, then the GRE pulse sequence is said to be spoiled. Spoiled GRE sequences are used in short-$TR$ sequences, which are suitable to obtain $T1$ weighted images. In this case, $TR$ may be shorter than $T2$ four or five times so that transverse magnetization would not decay fully near zero by the end of the pulse sequence and would affect following signals, thus producing artifacts. Active crushing of the transverse magnetization is achieved by the application of end-of-sequence gradient spoiler pulses or by using phase-cycled RF spoiling pulses. [2]

SSFP - *steady state free precession* - The greatest SNR per unit time is provided by a balanced SSFP with high flip angle and full rephasing of magnetizations in each $TR$ cycle. Because these sequences are prone to static-field inhomogeneity artifacts (banding), a deliberately non-balanced SSFP, characterized by constant gradient dephasing in each $TR$, is a similarly efficient option. The bright fluid signal is obtained, so this technique works well as a bright-blood technique in cardiac imaging. Multiacquisition SSFP is a good choice if banding artifacts cause a problem. SSFP-FID is a robust alternative when patient motion is a problem. [2]

Names of the common GRE pulse sequences vary with the MR equipment vendors. For example:

SPGR - *spoiled gradient echo* by General Electric = FLASH - *fast low-angle shot* by Siemens or T1-FFE - *T1 fast field echo* by Philips.

SSFP-FID or gradient echo = GRASS - *gradient recalled acquisition in the steady state* by General Electric or FFE - *fast field echo* by Philips or FISP - *fast imaging with steady (-state free) precession* by Siemens. [2]

## SE derived pulse sequences

RARE - *rapid acquisition with relaxation enhancement* - is using a train of refocusing pulses in order to produce multiple RF spin echoes. Each of echoes is distinctively spatially encoded which provides reduction of the scan time due to multiple k-space lines sampling. [2]

EPI - *echo planar imaging* - is one of the fastest MRI pulse sequences. The main difference is the application of a series of bipolar readout gradients (a gradient echo train) and phase-encoding gradients with multiple k-space lines sampled under a FID or an RF spin echo. That's why the EPI pulse sequence data acquisition is even faster than RARE (using RF spin echo train). [2]

## IR derived pulse sequences

STIR - *short tau (or TI) inversion recovery* - uses TI typically from 150 to 170 ms to null the lipid signal which has the $T1$ relaxation time around 230 ms. This lipid signal suppression makes STIR an important clinical application of IR based on the difference in $T1$ between water and lipid. The lipid signal suppression can increase evidence of lesions embedded in fat. [2]

FLAIR - *fluid attenuated inversion recovery* - can, similarly as STIR nulls lipid signal, null the hyperintense fluid (e.g. cerebrospinal fluid, CSF) signal in $T2$ weighted images. This technique is widely used in neuroradiologic diagnosis for it's ability to gain $t2$ contrast among tissuer different from CSF such as brain parenchyma and a majority of lesions. [2]

Multiple IR - is using two IR pulses (*double IR* - DIR), the first one spatially non selective following the second one slice selective IR pulse. This is applied in black-blood MR angiography to null the signal from moving blood. Sometimes the *triple IR* - TIR is used to null both blood and lipid signals. [2]

### Combined pulse sequences

GRASE - *gradient and spin echo* - or TGSE - *turbo gradient spin echo* - is a combination of EPI and RARE pulse sequences using a train of RF refocusing pulses each combined with a train of alternating polarity readout gradients. [2]

## 2.3 Regularity replaced by pseudorandomness

Parallel MRI is using data acquired from multiple-coil arrays with reduction of scan times (by skipping certain k-space measurements). The reconstruction process can either be realised by filling in the missing k-space data (simultaneously acquired using multiple coins) or by unfolding aliased undersampled images. Parallel MRI is the most used current routine in clinical examinations. However, the limitations of this technique are the number of coil element and the design of coil arrays which affect the maximum acceleration of parallel imaging.

Nowadays, deep learning has quickly expanded to many modern scientific disciplines, including MRI. Deep learning is a part of machine learning using combination of model representations to learn complex functions from simple linear features in the beginning to more sophisticated features in deeper layers. To achieve this deep learning is using a multiple layer neural network inspired by the anatomy and functions of neurons.

MR Fingerprinting (MRF) [9] was introduced in 2013, since then MRF emerged as a method for MR acquisition, reconstruction, and analysis because of its faster, more efficient, and simultaneous quantification of multiple tissue properties from a single rapid acquisition. MRF uses pseudorandomized acquisition parameters, for example repetition times and flip angles, instead of steady-state signals, and template matching algorithm to generate quantitative tissue parameters and unique signal signatures, or 'fingerprints', for different tissue types.

These fingerprints are captured as undersampled images per time point (scan acceleration, signal matching is robust to incoherent aliasing artifacts). Quantitative maps are reconstructed by matching measured signal evolutions to a dictionary of simulated signals (a huge look-up table of all likely resonance signals derived using the Bloch equation simulations). Moreover, this dictionary generation and signal matching can be in some circumstances slow and memory-intensive process. Recently, several groups have proposed using state-of-the-art methods that employ machine learning to accelerate the extraction of quantitative maps from the MRF data. [16]

MRF method includes MRF pulse sequence, data sampling, MRF dictionary, and pattern recognition. MRF pulse sequence differs from standard mapping tech-

niques and qualitative scans by using acquisition settings that change throughout the scan to enhance the sensitivity to $T1$ and $T2$. Exploited sequences have variable flip angles, repetition time, echo time, or different imaging readouts. Afterwards the measured signal is used for identification of tissue property values. These data are collected at a high temporal resolution in k-space. Typically, sampling is accomplished by non-Cartesian trajectories, such as spiral, radial, rosette, or echo planar imaging (EPI), because of their incoherent aliasing when undersampled, frequent sampling in the k-space centre, robustness in motion, and efficient k-space coverage. MRF dictionaries are generated from known pulse sequence parameters and the discrete set of tissue property values by Bloch equation simulation or extended phase graphs. In the end, the measured signal is compared with the dictionary using vector-dot product. The dictionary entry with the highest dot product is deemed the best match and the parameters associated with that entry are assigned to the voxel.

# 3 Reasons for relaxometry

In this chapter are described reasons for MR relaxometry

- scanner-independent diagnostics, interinstitutionally transferrable knowledge
- MRI contrast for discrimination of tissues, optimization of MRI pulse sequences
- intermediary parameter reflecting contrast agent concentration
- explanatory role in pathophysiology research

## 3.1 Scanner-independent diagnostics, interinstitutionally transferrable knowledge

Magnetic resonance imaging is based on the magnetic properties of tissues. [8] Compared with other imaging modalities such as computed tomography (CT) or positron emission tomography (PET), MRI offers superior soft-tissue characterization and more flexible contrast mechanisms without radiation exposure. This means that MRI is non-invasive technique serving to evaluation of tissues even better than CT regarding contrast in soft tissue via response of protons in a strong external magnetic field to a radiofrequency (RF) pulse. MRI allows acquisitions of functional, hemodynamic, and metabolic information in addition to high-spatial-resolution anatomical images for a comprehensive examination.

Conventional MR images (providing excellent tissue contrast) are limited to the qualitative assessment of contrast-weighted images [23], because the quantitative metric for absolute interpretation of pixel signal intensity is dependent on particular hardware and software settings. Then the comparison of MR images subjective and dependent on the MR protocol. On the contrary quantitative MRI refers to measurement of the fundamental parameters as the relaxation times T1, T2, T2* (the times taken for relaxation of proton spin precession in the longitudinal and transverse planes) reflecting biophysical features that contribute to MR signal. These maps are independent on the MR protocol and their physical interpretation express absolute units.

In a clinical sphere [13], there is increasing value of MR relaxometry in diagnosis, stage evaluation, and monitoring of various human diseases, including neurocognitive disorders, neurodegeneration, cancer, myocardial and cardiovascular abnormalities, degenerative musculoskeletal diseases, and hepatic and pulmonary diseases. MR relaxometry could enables early identification of pathologies, delivers more specific information about tissue composition and microenvironment, and provides better sensitivity to different diseases compared with conventional MR images.

Quantitative imaging is providing many advantages as removal of influences unrelated to tissue properties (operator dependency, different scan parameters, various magnetic field, image scaling, ...), comparison of different measurements (between different patients or the same patient during certain time period) within multi-institutional studies.

Still there are well known limitations of MR relaxometry, which include long scan times because of the necessity of repeated acquisitions with varying sampling parameters, sensitivity to different system imperfections, and clumsy post-processing. But lately these imperfections have been improved by faster imaging sequences, more efficient sampling trajectories, better gradient systems, and more. Moreover, the introduction of techniques based on fingerprinting and deep learning allowed more efficient generation of multiple MR parameters from a single acquisition. Deep learning in quantitative MRI has recently attracted considerable attention in the MRI community especially in research, e.g., image reconstruction, analysis and processing, and image-based disease diagnostic and prognosis.

## 3.2 MRI contrast for discrimination of tissues; optimization of MRI pulse sequences

Traditional methods for quantitative MRI generate maps of pixel representations by absolute measurement of a tissue property, such as T1 or T2. These features are acquired sequentially at particular time points after an inversion or saturation pulse to vary the T1 contrast or with different echo times (TE) after a 90° excitation to obtain different T2 contrast. After acquisition, the signal intensity in each pixel is fitted to a simple model, such as exponential recovery for T1 or exponential decay for T2, then a quantitative map is extracted.

However, traditional methods stand on accuracy, precision, and reproducibility. Resulted values are dependent on chosen pulse sequences, image reconstruction techniques, or signal models. They also can be affected by motion artifacts such as bulk patient movement, respiration, cardiac motion, peristalsis, or flow. In addition, there is a persistent disadvantage of long scan times, which may be uncomfortable for patients and limit scan throughput. As we can see, even the same method may produce different measurements across scanners. That is why we want to unify quantitative results of individual measurements across the scanners, workplaces, or even institutions to help radiologists better reflect pathology, make more informed diagnosis, directly compare images, and reduce subjectivity.

Moreover, the increasing interest in the use of biological markers [19] in clinical diagnosis over the past two decades made quantitative mapping techniques even

more desired to complement qualitative imaging. Biomarkers such as water diffusion constants, blood flow fields, fat fraction, tumour volume, brain volume, functional network connectivity, and more, are objectively measured parameters. To reach this objectivity, it is necessary to comply the use of a standard system phantom, a calibration/standard reference object, to assess the performance of an MRI machine. Then a great reliability and comparability of the data can be achieved.

## 3.3 Intermediary parameter reflecting contrast agent concentration

MRI contrast agents [27] first appeared shortly after the clinical introduction of MRI in 1981. A few years later, in 1988, the first contrast agent for clinical use was born – Gd-DTPA. These chemicals are used in general because of their impact on T1 and T2 relaxation times which increase the contrast between normal and abnormal tissues in the minutes after injection. Positive agents are mostly paramagnetic contrast agents which increase signal intensity (shorten T1 of neighbouring water protons) and display brighter in T1-weighted images. On the other hand, negative agents such as dysprosium, superparamagnetic and ferromagnetic agents reduce signal intensity by shortening T2 which appear darker in T2-weighted images.

Nowadays are contrast agents under strict scrutiny because of their safety for clinical use. The contrast agents can be divided by their chemical composition into two groups: paramagnetic compounds (including lanthanide ions such as gadolinium or manganese) and superparamagnetic iron oxides (as iron and platinum). To prepare nontoxic contrast agents based on metallic ions, the concept of chelation is widely used. [26]

MRI contrast agents can be administered intravenously, orally, or by inhalation. The intravenous route of administration is more useful, used contrast agents are paramagnetic compounds (ionic gadolinium and non-ionic gadodiamide and gadoteridol). The oral administration is appropriate for GI tract scans and includes Gadolinium-based agents (GBCAs), SPIOs, manganese-based agents and barium sulfate suspensions. Ventilation contrast agents are inhaled to improve the diagnostic value of MRI for the lungs. These include Gadolinium-based aerosols and oxygen gas, both paramagnetic, and hyperpolarized gases (3He, 129Xe) and inert perfluorinated gases (SF6).

GBCAs [26] are so successful because of their provision of non-invasive technique for detection of blood brain barrier (BBB) disruption. GBCAs do not cross the BBB, that is why the contrast enhancement of the brain can only be caused by pathologies (e.g., multiple sclerosis, cancer, or stroke). GBCAs is also used in detection of

increased vascular permeability, breast cancer, blockages or aneurysms in blood vessels, or to measure regional perfusion of heart.

The contrast agents are divided into three groups [27] according to biodistribution and application: extracellular fluid (ECF), blood pool and target/organ-specific agents. ECF agents are the most used agents based on distribution within the extracellular space with little or no interactions with proteins or cells. Blood pool contrast agents (BPCAs) are, after injection, restricted to the intravascular space and providing longer view for imaging arteries and veins than ECF agents because of their longer remaining in intravascular space. Targeted and organ specific contrast agents, such as iron oxides and liposomes, can target specific tissues, for example the liver, spleen, or lymph nodes.

The ECF agent's distribution [26] within tissues is observed using great contrast between anatomical structures and pathophysiology. To achieve biochemical specificity two approaches are available: to couple the contrast agent to a targeting vector to localize the agent to a specific protein or cell type, or to modulate the contrast generating signal in response to some stimulus.

## 3.4 Explanatory role in pathophysiology research

Quantitative relaxometry has explanatory role in pathophysiology research studies in the brain, body, and heart. [23]

Brain pathology is often represented by prolongation of the T1, T2, and T2*, which can even refer to autism, dementia, and Parkinson disease. The greatest exposure to relaxometry studies have brain tumours, stroke, epilepsy, and multiple sclerosis. Brain tumours are usually studied using qualitative MRI, but quantification can expose tumour type by length of T1 (glioblastomas have the longest T1, meningiomas have shorter T1, but still longer than healthy white matter). Stroke is characterized by T1 and T2 prolongation and relaxometry maps can even distinguish savable and nonsavable tissues. Epilepsy is described in relaxometry maps by increased T1 and T2 values in the temporal lobe. Multiple sclerosis is described by changes in the relaxation times in both grey and white matter.

Quantification of relaxometry in the body is exploited to characterization of iron overload, cartilage disease, injuries and infections, and cancer. Iron overload is a result of accumulation of iron in the liver and spleen as a result of frequent blood transfusions (to treat anemia), in evaluation of iron levels in extra-hepatic organs (as liver, spleen, pancreas, and kidney) relaxometry has replaced biopsy procedures. In organs with iron overload the relaxation times are shorter than in those with normal values. Cartilage diseases including osteoarthritis, rheumatoid arthritis, and other degenerative conditions of the cartilage can not only be detected in their early

phases but also can be treated using relaxometry. Injury and infection assignment using quantitative relaxometry is occasionally used in clinic. Cancer is normally detected by quantitative relaxometry through contrast-enhanced protocol.

The contrast of soft tissues provided by relaxometry can describe differences between pathological and normal heart muscle. Moreover, quantitative relaxometry can monitor treatment development and rate severity of disease. The quantitative relaxometry is exploited in the management of patients suffering from cardiac iron overload, can recognise the state of the tissue damage after acute myocardial infarction, monitor edema or inflammation, identify intramyocardial hemorrhage, and more.

# 4 Materials and methods

## 4.1 MRI experiment

First imaging protocol was performed on a phantom with eight test tubes containing different concentrations of Gd-nanoliposomes and control samples as following, see illustrations in Fig. 5.11. Second experiment was performed on fixed rat brain by paraformaldehyde in an agar gel, see illustrations in Fig. 5.12.

Used RARE sequences were performed with following parameters: TR = [0.15; 0.282; 0.435; 0.615; 0.835; 1.118; 1.513; 2.176; 5] s, TE = [0.015; 0.03; 0.045; 0.06; 0.075; 0.09; 0.105; 0.12] s.

Tab. 4.1: Phantom contents

| Sample | Contents | Gd [mmol/l] |
|---|---|---|
| 1 | Gd-nanoliposomes | 150 |
| 2 | Gd-nanoliposomes | 75 |
| 3 | Gd-nanoliposomes | 37.5 |
| 4 | Gd-nanoliposomes | 18.75 |
| 5 | Gd-nanoliposomes | 9.375 |
| 6 | Buffer | 0 |
| 7 | Physiological saline | 0 |
| 8 | Vegetable oil | 0 |

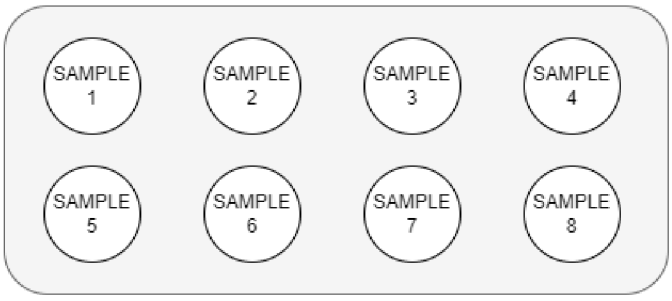


Fig. 4.1: Phantom composition.

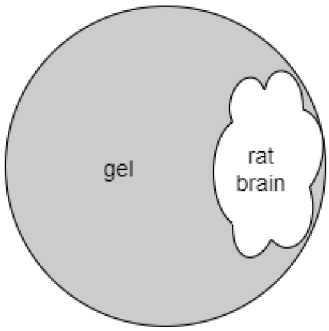


Fig. 4.2: Rat brain fixed in agar gel.

## 4.2 Methods

Usually the quantitative MRI techniques are provided using $T2$ and/or $T1$ weighted images where the contrast is based on relative contributions from different tissues. Also the relaxometry maps can be created based on the relaxation time itself. These can be figured considering each one of the relaxation times separately or together. The principles of individual and simultaneous fitting of relaxation times $T1$ and $T2$ are presented below.

Relaxometry maps can be generate either by spin-echo or gradient-echo sequences with two or more different $TE$ and $TR$, in general, these sequences are called multi-spin-echo sequences (MSE). The noise is bigger when the magnetizing field is greater and the sensitivity of the map depends on many acquired parameters such as type of sequence, $TR$, $TE$, number of images and the model function used for data fitting. Increasing TR increases signal-to-noise ratio (SNR) and the larger number of $TE$s the better is SNR. [5]

### Algorithm implementation

The implemented algorithm, see illustrations in Fig. 4.3, uses multidimensional data from Gd-nanoliposomes relaxation study performed on Bruker Biospec 9.4 T scanner at ÚPT AV ČR, v. v. i. Data are loaded using already developed library from ÚPT AV ČR developer Tomáš Pšorn. This algorithm for quantitative relaxometry is the next step in development of independent software for MR images viewing and processing.

First the necessary libraries, i.e. `numpy`, `scipy.optimize`, `matplotlib.pyplot`, and `brukerapi.dataset`, and data from dataset are loaded. Data dimensions are detected - the first two dimensions describe the position of pixel in 2D space, the third one is definition of slice in 3D space (not in our study), the fourth and fifth dimension contains TE and TR data. Then data for $T1$ relaxometry fitting are

obtained as `dataset.data[y, z, 0, te, :]`, or `dataset.data[y, z, 0, :, tr]` for $T2$ fitting, for each pixel [y, z] and each $TE$ or $TR$.

After the initialization of starting matrixes for writing resulted fitted parameters and deviations, the nested for cycle is initiated for all y, z, and $TE$s or $TR$s. Data are sent into fitting process only if they are bigger than expected noise value. The selection of the model function is dependent on required relaxometry parameters, such as $T1$, $T2$, or both. The model function is based on least squares function implemented in `scipy.optimize` library. Fitting mechanisms and error estimation are described below. Results are written into matrixes (one for each parameter).

The resulting images are shown using `matplotlib.pyplot` library in a figure for all parameters and deviations simultaneously and individually. The results can be also displayed for an individual pixel comparing acquired relaxometry data and fitted resulting curves.

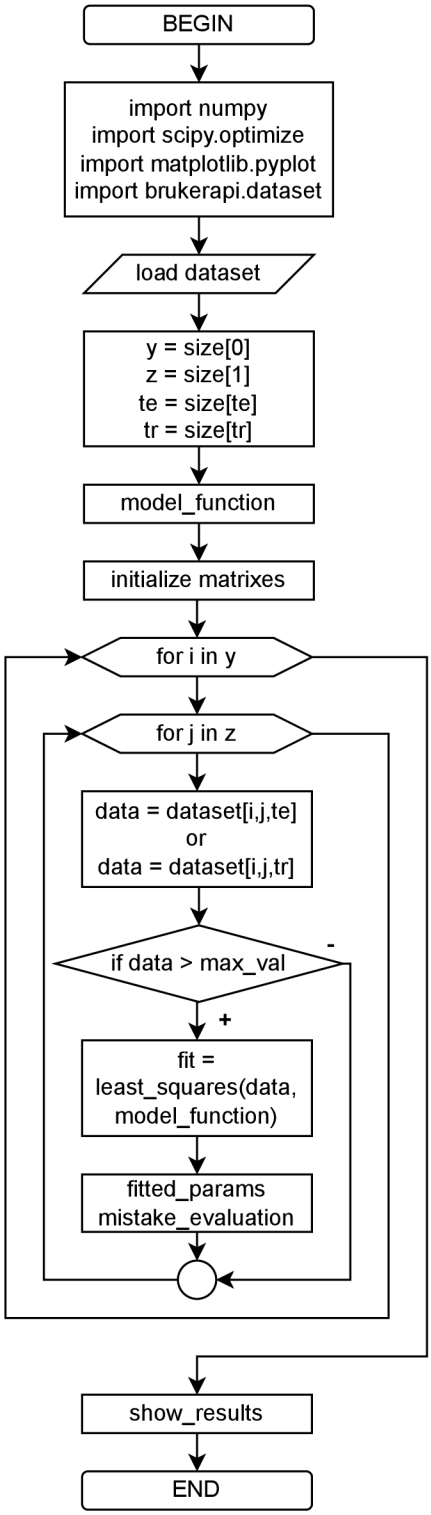


Fig. 4.3: Process flow diagram.

## Individual T2 fitting

Since 1971, when the first publication of $T2$ relaxometry from Damadian [11] was published, there are efforts to determine the $T2$ as bio markers for various diseases and as a parameter for prognosis and therapy control.

Usual approach to determine $T2$ relaxometry is from data acquired using multiple single Spin Echo (SE) sequences with different echo times (TE). Generally, Multi Spin Echo (MSE) sequences are used in clinical sphere because of their possibility of multiple echoes within one acquisition depending on the number of 180° refocusing pulses. Echo train length (ETL) is than term for the number of echoes and echo spacing (ESP) is the time between echoes.

Major reasons for incorrect $T2$ times are imperfect slice excitation profiles and issues with B1 inhomogeneities yielding low refocusing flip angles (FA). The correction of B1 field inhomogeneities is usually computationally intensive and the implementation is complicated. Therefore, the post-processing and data fitting can eliminate some of these known systematic errors using these techniques [24]:

1. Data fitting of all echoes with an exponential curve:

$$S(TE) = Ae^{-TE_k \cdot R2} \tag{4.1}$$

   where $A$ is factor of proton density and signal gain or attenuation by the scanner's hardware/software, $TE$ is the echo time and $k = 1, 2, \ldots$

2. Data fitting of all echoes with an exponential curve with adjusted offset (baseline):

$$S(TE) = Ae^{-TE_k \cdot R2} + C \tag{4.2}$$

   where $C$ is the offset representing non-zero baseline, when the $T2$ decay does not tend towards zero, but to an asymptote $> 0$. The offset represents the noise (can be also caused by $B1$ inhomogeneities and imperfect refocusing pulses). The more FA deviates from 180° the higher the offset is. The highest offset is while ETL and ESP are low, which is usually used in clinical scanners to shorten the acquisition time. The offset also helps to compensate the oscillation between even and odd echoes.

3. Discarding of the first echo:

$$S(TE) = Ae^{-TE_k \cdot R2} + C. \tag{4.3}$$

   By discarding the first echo for curve fitting we reduce the signal oscillations in the early echoes, which is a major source of error in $T2$ quantification. By discarding the first echo and adding the offset as a fitting parameter we

should get rid of the most of the systematic error and provides fast and reliable post-processing method.
Regardless, this method does not completely compensate the errors of $T2$ caused by $B_1$ inhomogeneities, these should be reduced while acquiring using advanced acquisition techniques such as using a larger spatial width of the refocussing pulse compared to the excitation pulse or by parallel transmission.

### Individual T1 fitting

Exact determination of $T1$ longitudinal relaxation time of brain tissues is important in multiple clinical applications such as distinguish several neurological disorders, e.g. multiple sclerosis and Parkinson's disease, delineation of brain structures and differentiation of pathologies. Moreover, the extraction of pharmacokinetic parameters requires accurate $T1$ values. Finally, while approximating the $T2$ values in certain methods the knowledge of $T1$ values leads to better results. [22]

For T1 fitting was used the following model function using data fitting of all repetition times with an exponential curve:

$$S(TR) = A(1 - e^{-(TR_m - TE_K)\cdot R1}) + C \tag{4.4}$$

where $A$ is factor of proton density and signal gain or attenuation by the scanner's hardware/software, $TR$ is the repetition time, $m = 1, 2, \ldots,$ length(TR), $TE_K =$ max(TE) and $C$ is the offset representing non-zero baseline.

### Simultaneous T1 and T2 fitting

Two variable model function for $T1$ and $T2$ simultaneous fitting:

$$S(TE, TR) = A(1 - e^{(-TR_m - TE_K)\cdot R1})e^{-TE_k \cdot R2} + C \tag{4.5}$$

where $A$ is factor of proton density and signal gain or attenuation by the scanner's hardware/software, $TR$ is the repetition time, $m = 1, 2, \ldots,$ length(TR), $TE_K$ = max(TE), $TE$ is the echo time, $k = 1, 2, \ldots,$ length(TE) and $C$ is the offset representing non-zero baseline.

## 4.3 Noise estimation

Noise in data can be estimated using a great deal of methods. Unfortunately, there is not the most universal one.

To estimate noise in phantom data, the values from the edge of the image were chosen (all left edge, right edge, bottom edge and top edge values). These values

should be independent on the phantom data values. To verify this statement, vector of values from which the noise is assessed is figured in the beginning of the algorithm. User can check up if there is a ghost or phantom overrun and can adjust the area to calculate the assumed noise value.

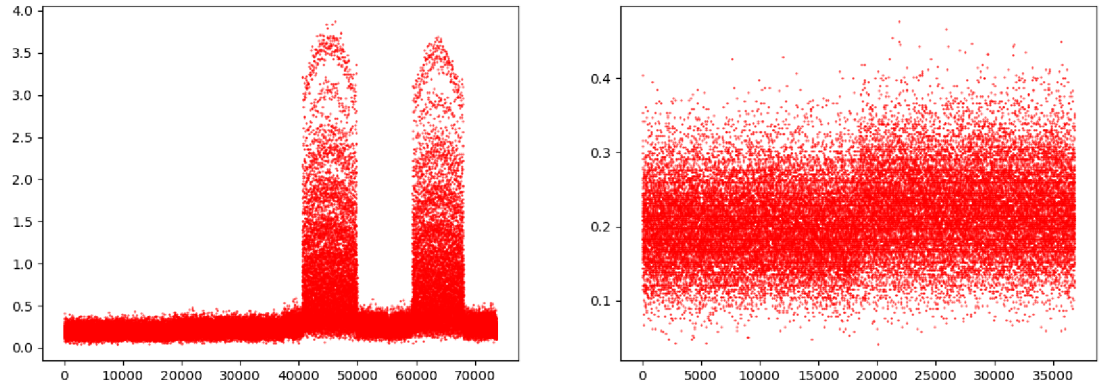


(a) incorrect - all edges, phantom overrun (b) correct - top and bottom edge

Fig. 4.4: Noise estimation area in fixed brain data.

## 4.4 Standard deviation estimation - locally linearized model

A simple estimation of the standard deviation of the estimated parameters can be based on a linearized model of the parameter-to-data mapping in the neighborhood of the solution, and the knowledge of data noise, assumed to be Gaussian and white with zero mean.

Let us assume that the mapping of parameters $x = (x_1, ..., x_P)^T$ and experimental conditions $c = (c_1, ..., c_Q)^T$ to data $y = (y_1, ...y_N)^T$ is described by multiparametric mapping $\Psi$, i.e.

$$y = \Psi(x, c). \tag{4.6}$$

In practice the measurement is repeated with a limited number of experimental conditions, $c_1, ..., c_K$, so that the k-th data value obtained with experimental conditions $c_k$ is supposed to be a random variable whose expectation is

$$y_k = \Psi(x, c_k), \tag{4.7}$$

and so depends on the unknown parameters $x$. In a limited neighborhood of the true parameters $x_0$, the sensitivity of the model data to a parameter change from

$x_0$ to $x_0 + \Delta x$ can be supposed to be sufficiently described by the first-order Taylor expansion of mapping $\Psi$, i.e.,

$$y_k + \Delta y = \Psi(x_0 + \Delta x, c_k) = \Psi(x_0, c_k) + D\Delta x, \tag{4.8}$$

where

$$y_k = \Psi(x_0, c_k) \tag{4.9}$$

and

$$D_{np} = \frac{\delta \Psi n}{\delta x_p}. \tag{4.10}$$

This leads to a linear relationship

$$\Delta y = D\Delta x, \tag{4.11}$$

This relation can be used to estimate how data noise $\Delta y$ is transformed into parameter noise $\Delta x$. In this way, data noise limits the achievable precision of the fitted parameters $x$. Matrix $D$ can be decomposed by singular value decomposition:

$$\Delta y = USV^{HT}\Delta x, \tag{4.12}$$

where $U$ is unitary matrix ($m \times n$, where $m$ is number of $TEs$ ($TRs$, or $TE \cdot TR$) and $n$ is number of singular values $> 0$), $S$ is matrix of singular values sorted in descending order ($m \times n$, where $m = n =$ number of singular values $> 0$), and $V^H$ is unitary matrix ($m \times n$, where $m$ is number of singular values $> 0$, and $n$ is number of parameters). Then using matrix operations we get

$$V^{HT-1}S^{-1}U^{-1}\Delta y = \Delta x, \tag{4.13}$$

$$\Delta x = V^H S^{-1} U^T \Delta y, \tag{4.14}$$

$$std(n_k) = \sqrt{\sum D_{kl}^2 \varepsilon^2}. \tag{4.15}$$

1. **Individual T2 fitting**
   The basic consideration is that we measure a perfect spin echo with different $TE$ echo times. Ie. it can be a spin echo or (with a little good will) a series of spin echoes (RARE). It does not depend much on $TR$ and perfect relaxation, if we measure all echoes from the same dynamic balance. For $T2$ fitting the model function is used

$$f_k = \Phi(x, c) = \Phi((A, R2, C), TE_k) = Ae^{-TE_k \cdot R2} + C \tag{4.16}$$

then

$$D = \begin{pmatrix} \frac{\partial \Phi_1}{\partial A} & \frac{\partial \Phi_1}{\partial R2} & \frac{\partial \Phi_1}{\partial C} \\ \vdots & \vdots & \vdots \\ \frac{\partial \Phi_k}{\partial A} & \frac{\partial \Phi_k}{\partial R2} & \frac{\partial \Phi_k}{\partial C} \end{pmatrix} \tag{4.17}$$

where

$$R2 = 1/T2 \tag{4.18}$$

and

$$\frac{\partial \Phi_k}{\partial A} = e^{-R2 \cdot TE_k}, \tag{4.19}$$

$$\frac{\partial \Phi_k}{\partial R2} = -A \cdot TE_k \cdot e^{-R2 \cdot TE_k}, \tag{4.20}$$

$$\frac{\partial \Phi_k}{\partial C} = 1. \tag{4.21}$$

**2. Individual T1 fitting**

For $T1$ fitting the model function is used

$$f_k = \Phi(x, c) = \Phi((A, R1, C), (TR, TE_K)) = A(1 - e^{-(TR_m - TE_K) \cdot R1}) + C \tag{4.22}$$

then

$$D = \begin{pmatrix} \frac{\partial \Phi_1}{\partial A} & \frac{\partial \Phi_1}{\partial R1} & \frac{\partial \Phi_1}{\partial C} \\ \vdots & \vdots & \vdots \\ \frac{\partial \Phi_k}{\partial A} & \frac{\partial \Phi_k}{\partial R1} & \frac{\partial \Phi_k}{\partial C} \end{pmatrix} \tag{4.23}$$

where

$$R1 = 1/T1 \tag{4.24}$$

and

$$\frac{\partial \Phi_k}{\partial A} = 1 - e^{-R1 \cdot (TR_k - TE_K)}, \tag{4.25}$$

$$\frac{\partial \Phi_k}{\partial R1} = A \cdot e^{-R1 \cdot (TR_k - TE_K)} \cdot (TR_k - TE_K), \tag{4.26}$$

$$\frac{\partial \Phi_k}{\partial C} = 1. \tag{4.27}$$

3. **Simultaneous T1 and T2 fitting**
   In general, we could combine $TR$ and $TE$ in any way, but in RAREVTR it is natural to combine each $TR$ from a certain set with each $TE$ in the series in one scan. For simultaneous $T1$ and $T2$ fitting the model function is used

$$\begin{aligned} f_k &= \Phi(x, c) = \Phi((A, R1, R2, C), (TR, TE)) \\ &= A(1 - e^{(-TR_m - TE_K)\cdot R1})e^{-TE_k \cdot R2} + C \end{aligned} \tag{4.28}$$

   then

$$D = \begin{pmatrix} \frac{\partial \Phi_1}{\partial A} & \frac{\partial \Phi_1}{\partial R1} & \frac{\partial \Phi_1}{\partial R2} & \frac{\partial \Phi_1}{\partial C} \\ \vdots & \vdots & \vdots & \vdots \\ \frac{\partial \Phi_k}{\partial A} & \frac{\partial \Phi_k}{\partial R1} & \frac{\partial \Phi_k}{\partial R2} & \frac{\partial \Phi_k}{\partial C} \end{pmatrix} \tag{4.29}$$

   where

$$\frac{\partial \Phi_k}{\partial A} = 1 - e^{-R1\cdot(TR_m - TE_K)} \cdot e^{-R2 \cdot TE_k}, \tag{4.30}$$

$$\frac{\partial \Phi_k}{\partial R1} = e^{-R1\cdot(TR_m - TE_K)} \cdot (TR_m - TE_K) \cdot A \cdot e^{R2 \cdot TE_k}, \tag{4.31}$$

$$\frac{\partial \Phi_k}{\partial R2} = -A \cdot TE_k \cdot (1 - e^{-R1\cdot(TR_m - TE_K)} \cdot e^{R2 \cdot TE_k}), \tag{4.32}$$

$$\frac{\partial \Phi_k}{\partial C} = 1. \tag{4.33}$$

The model function $f$ is used to gain fitted parameters from the acquired data. The $M$ matrix, containing the partial derivations of the inverse function $\Phi$, is used to estimate the confidence interval of parameter fitting.

## 4.5 Standard deviation estimation - Cramér Rao lower bounds

The Cramér Rao lower bounds theory [6], [7] is based on the Likelihood function supposing that the noiseless data can be exactly modeled by model function $\widehat{y}_n$. The measured $n$-th data sample can be written as

$$y_n = \widehat{y}_n + b_n \tag{4.34}$$

where $b_n$ is the Gaussian-distributed noise $N(0, \sigma)$. Then the probability of $b_n$ (and $y_n$) is given by likelihood function

$$P(y_n|\mathbf{x}) = P(b_n|\mathbf{x}) = \frac{1}{\sqrt{2\pi\sigma^2}} e^{-\frac{b_n^2}{2\sigma^2}} \tag{4.35}$$

where $\sigma$ is the standard deviation of the noise. The joint probability function $P$, or likelihood function, for dataset $y = (y_1, y_2, ..., y_N)$ equals the product of the probability functions of all samples

$$P(\mathbf{y}|\mathbf{x}) = \prod_{n=1}^{N} P(y_n|\mathbf{x}) = \frac{1}{(2\pi\sigma^2)^{N/2}} e^{-\frac{\sum_{n=1}^{N} b_n^2}{2\sigma^2}} \tag{4.36}$$

The logarithm of this function (log-likelihood) is usually used.

$$\begin{aligned} L(\mathbf{y}|\mathbf{x}) = \log P(y_n|\mathbf{x}) &= -\frac{N}{2}\log(2\pi\sigma^2) - \frac{1}{2\sigma^2}\sum_{n=1}^{N} b_n^2 \\ &= -\frac{N}{2}\log(2\pi\sigma^2) - \frac{1}{2\sigma^2}\sum_{n=1}^{N}(y_n - \widehat{y}_n)^2 \end{aligned} \tag{4.37}$$

The key role in the estimation of fitting precision is played by the Fisher matrix. The Fisher matrix is defined by

$$F = E\left[(\tfrac{\partial L}{\partial \mathbf{x}})^T(\tfrac{\partial L}{\partial \mathbf{x}})\right] \tag{4.38}$$

where $E$ stands for the expectation value and $x = (x_1, x_2, ..., x_{Nx})$ represents the model parameters. The Fisher information matrix is then modified for real (bipolar) data:

$$\begin{aligned} F_{kl} = E\left[\tfrac{\partial L}{\partial x_k}\tfrac{\partial L}{\partial x_l}\right] &= \frac{1}{\sigma^4}\sum_{m=1}^{N}\sum_{m=1}^{N} E\left[((y_m - \widehat{y}_m)\tfrac{\partial \widehat{y_m}}{\partial x_k})((y_n - \widehat{y}_n)\tfrac{\partial \widehat{y_n}}{\partial x_l}\right] \\ &= \frac{1}{\sigma^2}\sum_{n=1}^{N}\frac{\partial \widehat{y}_n}{\partial x_k}\frac{\partial \widehat{y}_n}{\partial x_l} = \frac{1}{\sigma^2}\sum_{n=1}^{N} D_{nk}D_{nl}, \end{aligned} \tag{4.39}$$

$$D_{nk} = \frac{\partial \widehat{y}_n}{\partial x_k}, \tag{4.40}$$

$$F = \frac{1}{\sigma^2}\mathbf{D}^T\mathbf{D}. \tag{4.41}$$

The variance of the n-th parameter is found at the n-th position in the diagonal of inversion of $F$, which means that the standard deviation is estimated as

$$\sqrt{(F^{-1})_{nn}} \tag{4.42}$$

where

$$F^{-1} = \sigma^2(\mathbf{D}^T\mathbf{D})^{-1}. \tag{4.43}$$

# 5 Measurement results

In all measurements a volume transmit coil was used, providing fairly homogeneous flip angle in the whole sample.

## 5.1 Individual T2 fitting

Figures 5.1, 5.5 and 5.4 show the results of individual $T2$ fitting by model function

$$S(TE) = Ae^{-TE_k \cdot R2} + C \tag{5.1}$$

using all TE samples for each $TR$ individually. Because of the dependence of steady-state magnetization on $TR$, the SNR is higher in $TE$-decay series for higher $TR$. Then the resulting grayscale images display fitted model parameters $A$, $1/T2$, and $C$, and the estimates of the standard deviations of these parameters appropriate to the SNR present. The color images represent the fitted curves and the original data points for the first phantom - samples 1 and 8, see Fig. 5.2 and 5.3.

## Discussion - phantom

- Parameter $A$ describes the initial signal amplitude, as if no $T2$ decay existed. Therefore, higher values are expected and found where
  - proton density is high - identical for 1-7, different for 8
  - $TR$ is long - higher scan index
  - local coil sensitivity is high - center of image
- Relaxivity ($R2 = 1/T2$), as a property of the sample, should be found identical regardless of $TR$. High values correspond to samples with fast $T2$ relaxation: Fig. 5.1 shows, indeed,
  - shorter $T2$ (1/10 s = 100 ms) in samples with higher concentrations of the contrast agent (1)
  - long $T2$ (1/2.6 s = 380 ms) in saline with no contrast agent (6, 7)
  - shortest $T2$ (1/22 s = 45 ms) in oil (8)
- The DC offset value $C$, introduced only in order to adapt the theoretical model to the presence of unipolar noise in magnitude data, should not exceed the true noise level. This is
  - right for samples 1-7
  - wrong for oil (8)

  The reason for the anomaly in the oil sample is obviously in the insufficiency of the simple model 5.1 to accurately describe relaxation of oil, exhibiting many resonance frequencies and coupled resonances.

# Results - phantom

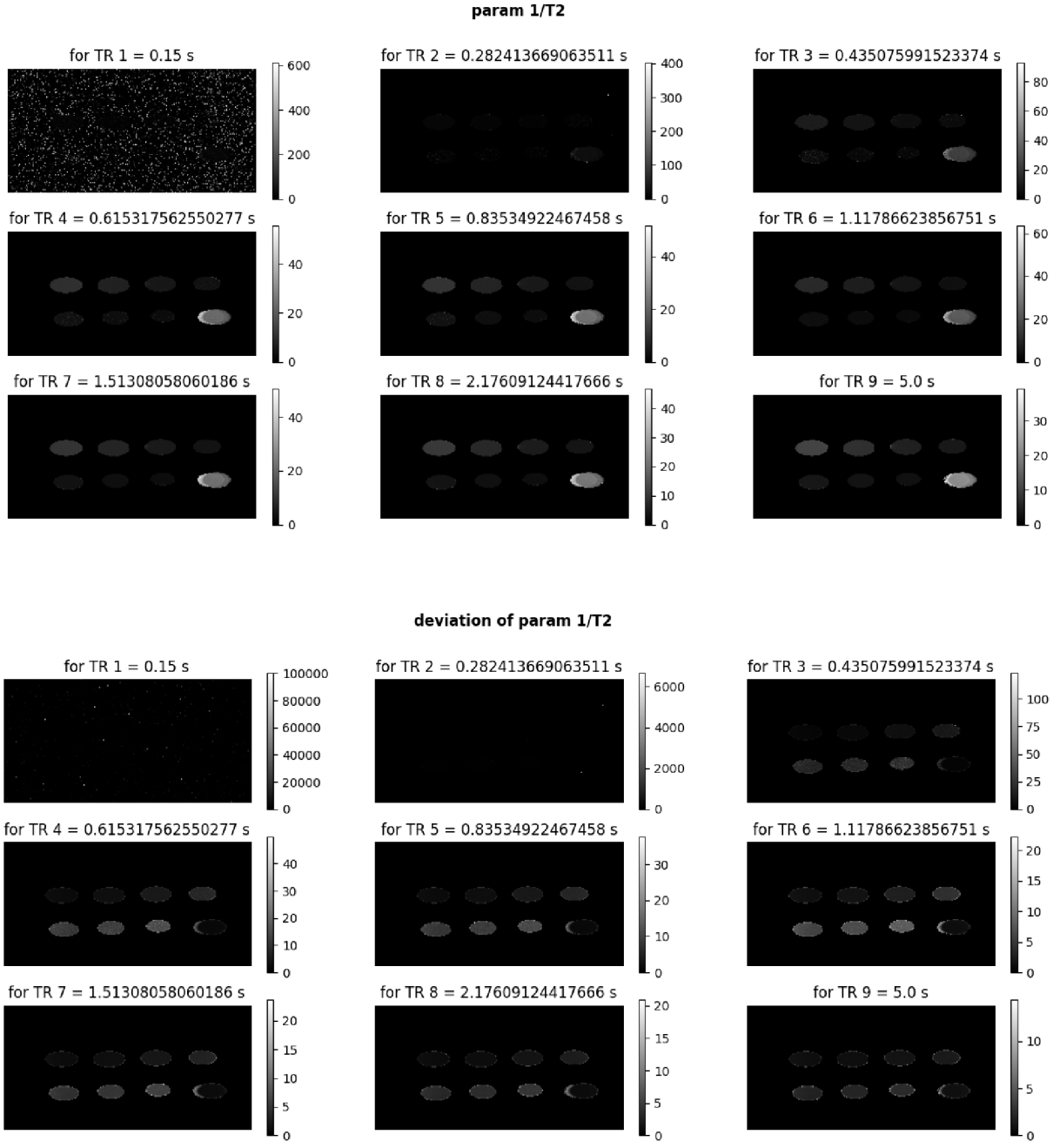


Fig. 5.1: Individual T2 fitting - parameter 1/T2.

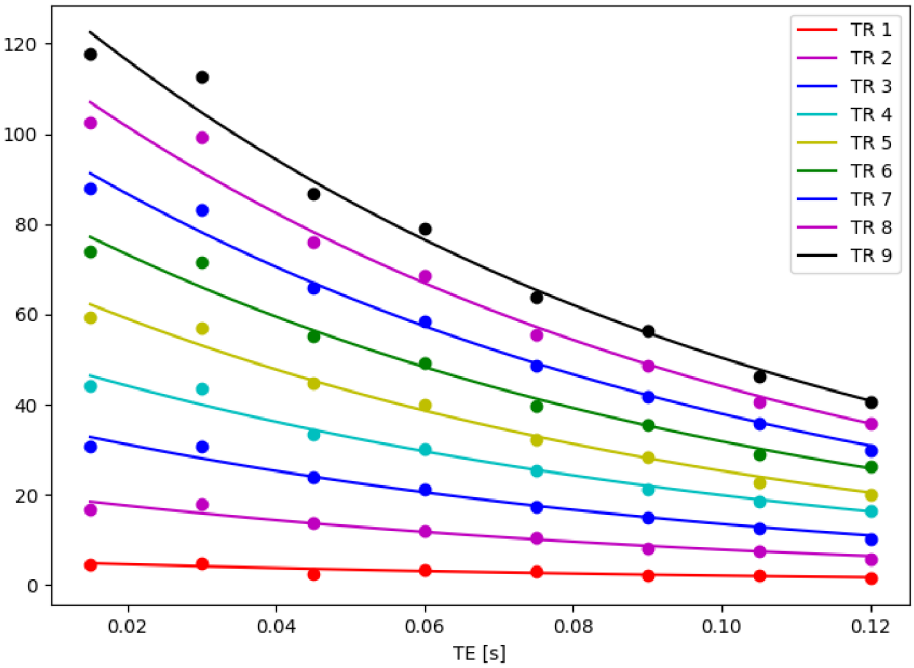


Fig. 5.2: Individual T2 fitting - sample 1.

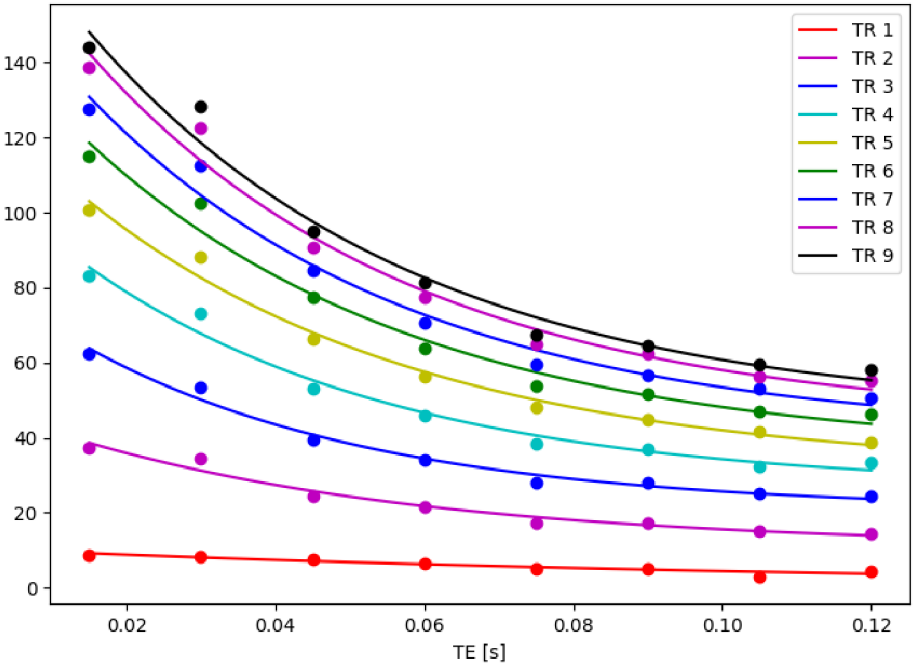


Fig. 5.3: Individual T2 fitting - sample 8.

# Results - fixed rat brain

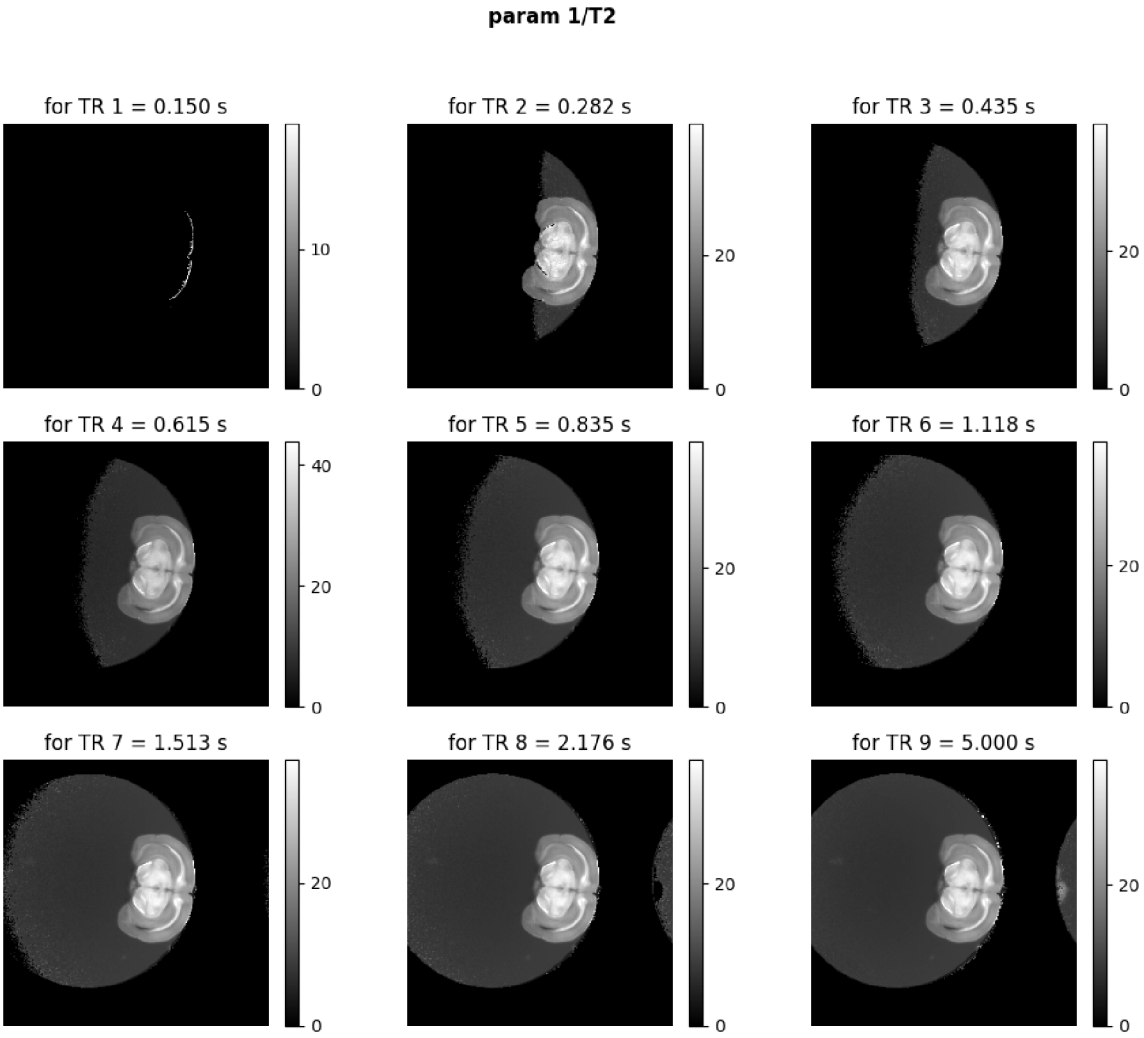


Fig. 5.4: Individual T2 fitting - fixed rat brain, whole FOV, parameter 1/T2.

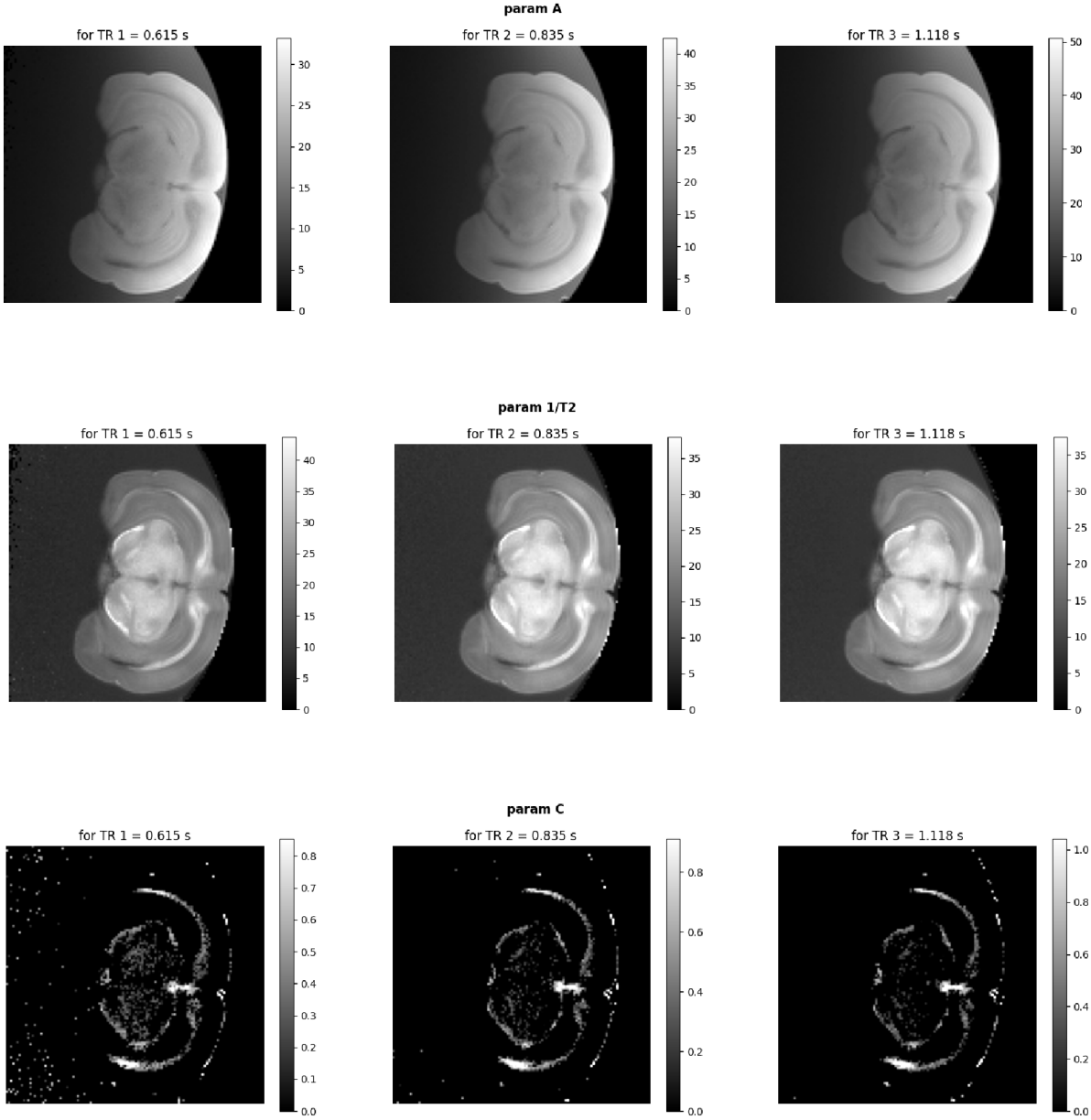


Fig. 5.5: Individual T2 fitting - fixed rat brain, all parameters, zoomed.

## 5.2 Individual T1 fitting

Figures 5.6, 5.9 and 5.10 show the results of individual $T1$ fitting by model function

$$S(TR) = A(1 - e^{-(TR_m - TE_K)\cdot R1}) + C \tag{5.2}$$

using all $TR$ samples for each $TE$ individually. Then the resulting grayscale images display fitted model parameters $A$, $1/T1$ and $C$, and the estimates of the standard deviations of these parameters appropriate to the SNR present. The color images represent the fitted curves and the original data points for the first phantom - samples 1 and 8, see Fig. 5.7 and 5.8.

## Discussion - phantom

- Higher values of parameter $A$ are expectable and found
  - in samples with higher proton density - identical for 1-7, different for 8
  - in measurements with shorter $TE$ - lower scan index
  - in areas with higher detection coil sensitivity
- Identical value of $T1$ should be found regardless of the $TE$ value used (albeit the lower SNR at higher $TE$ values may result in noisier $T1$ maps). High relaxivity ($R1 = 1/T1$) corresponds to fast $T1$ relaxation. The values found correspond to the expectations:
  - short $T1$ (1000 ms) in samples with higher concentration of contrast agent (1)
  - long $T1$ (4500 ms) for zero concentration (6, 7)
  - low $T1$ (670 ms) in the fast relaxing oil
- The DC offset $C$, here again, is an artificial adjustment of the theoretical model to the noisy reality. It should not exceed the noise level, which is
  - right for 1-7
  - wrong for oil (8)

  The offset $C$ again reflects the anomalous steady-state.

# Results - phantom

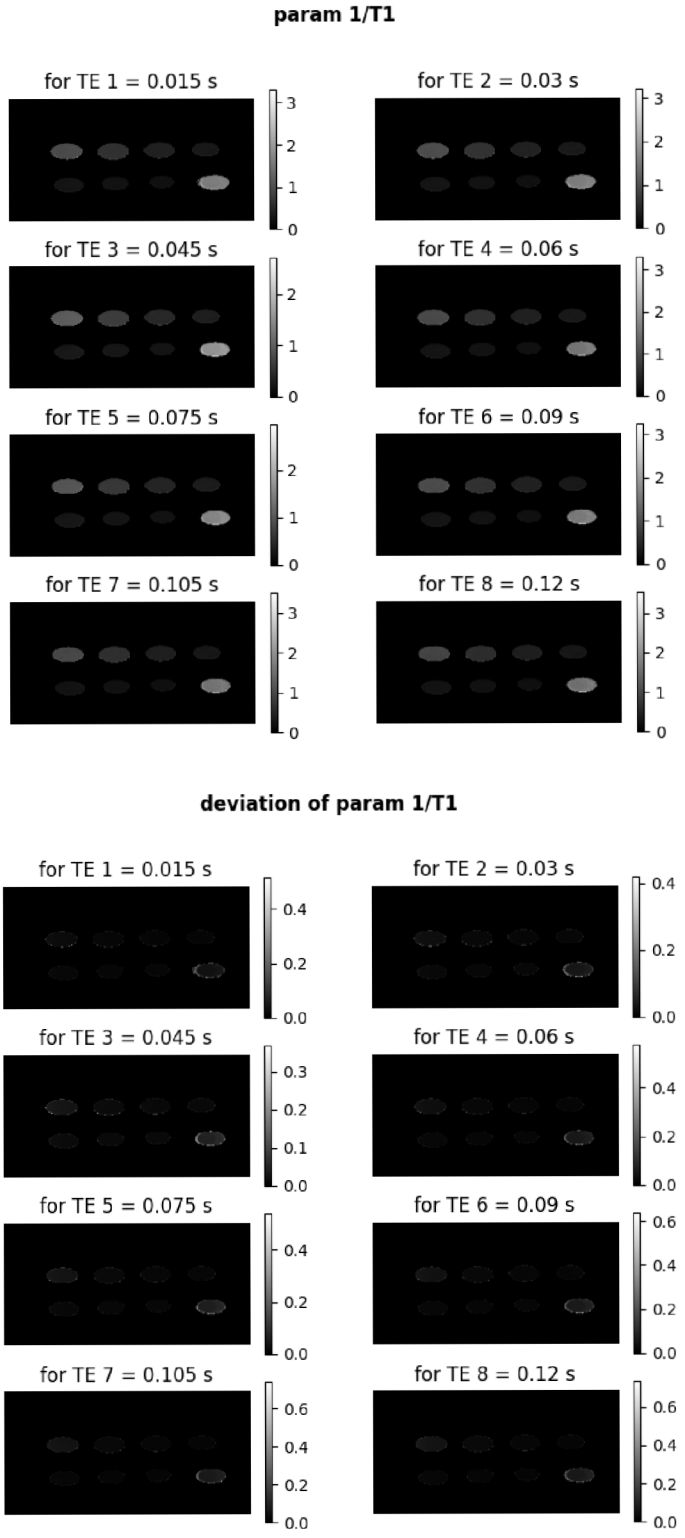


Fig. 5.6: Individual T1 fitting - parameter 1/T1.

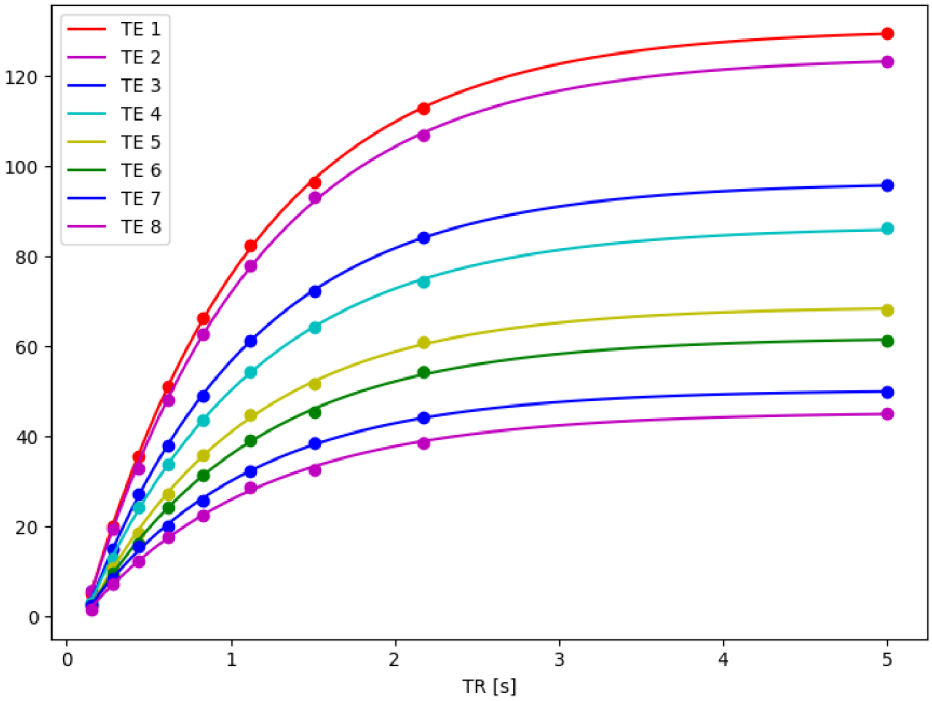


Fig. 5.7: Individual T1 fitting - sample 1.

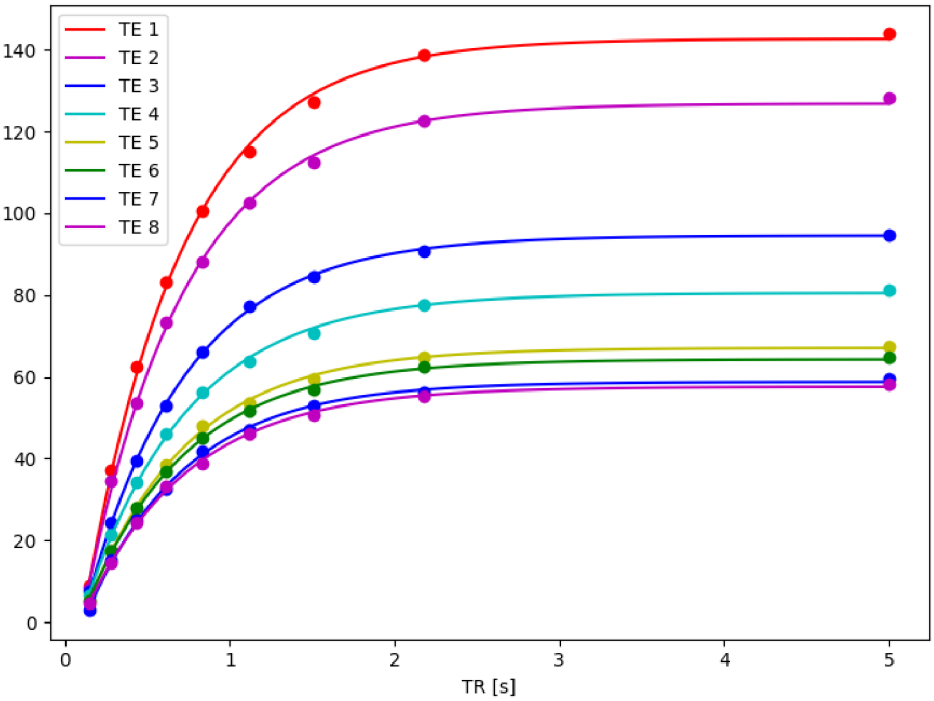


Fig. 5.8: Individual T1 fitting - sample 8.

# Results - fixed rat brain

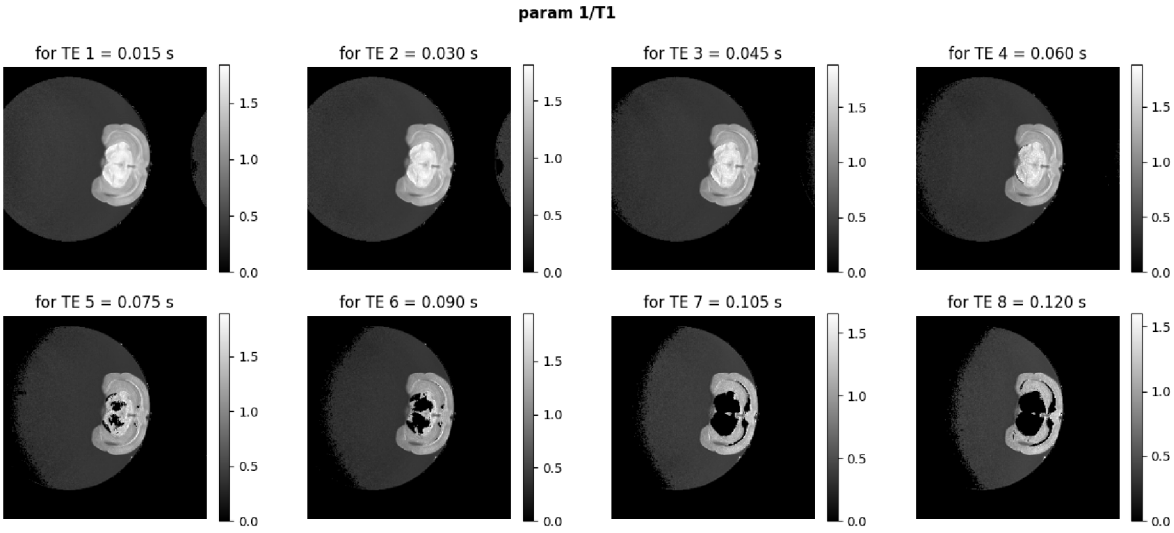


Fig. 5.9: Individual T1 fitting - fixed rat brain, whole FOV, parameter 1/T1.

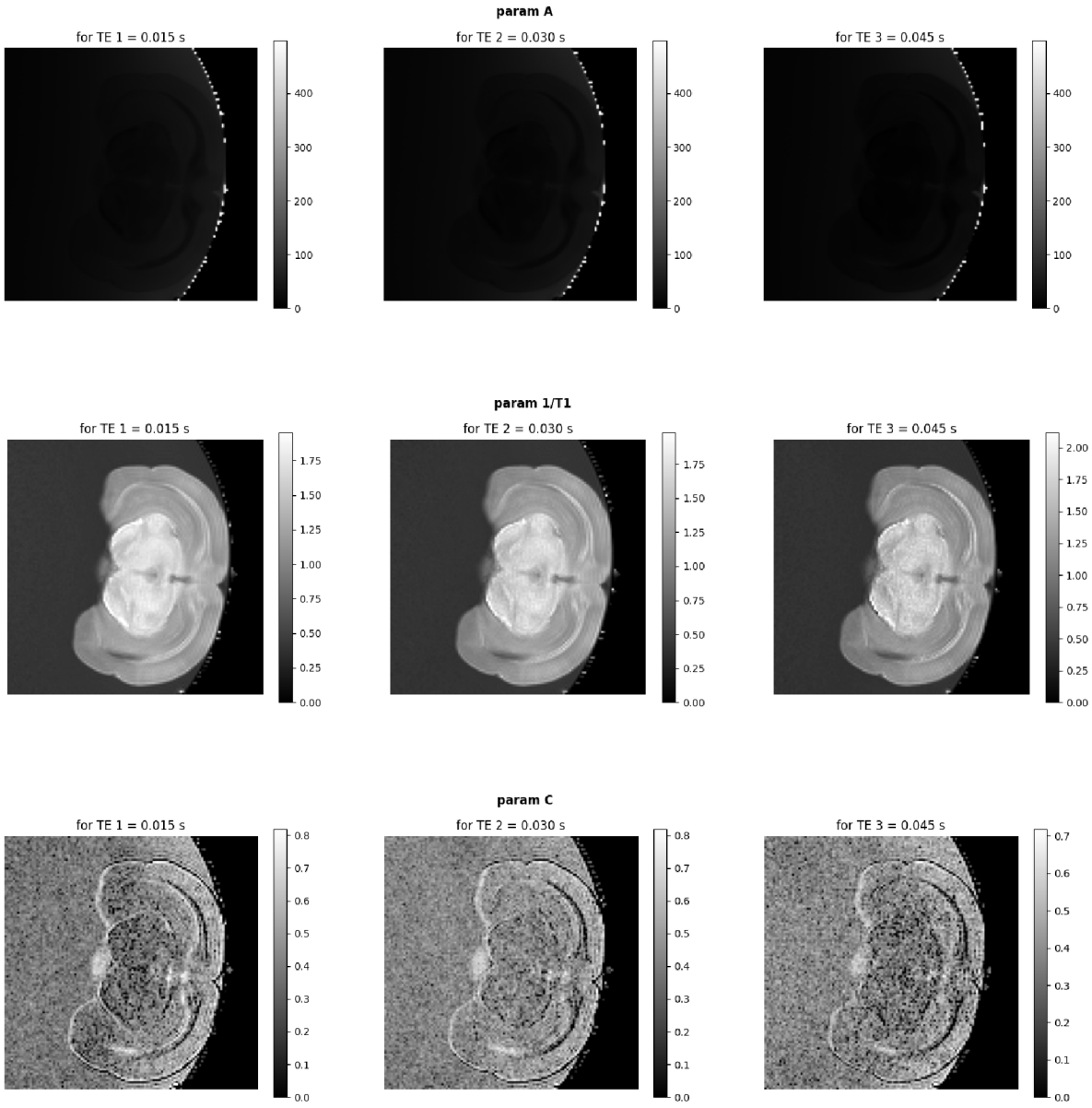


Fig. 5.10: Individual T1 fitting - fixed rat brain, all parameters, zoomed.

## 5.3 Simultaneous T1 and T2 fitting

Figures 5.11 and 5.12 show the results of simultaneous $T1$ and $T2$ fitting by model function

$$S(TE, TR) = A(1 - e^{(-TR_m - TE_K) \cdot R1}) e^{-TE_k \cdot R2} + C \tag{5.3}$$

then the resulting grayscale images display fitted model parameters $A$, $1/T1$, $1/T2$ and $C$, and the estimates of the standard deviations of these parameters appropriate to the SNR present.

## Discussion - phantom

Comparing the resulted values of fitted parameters obtained from the two methods (individual or simultaneous fitting) we get the following conclusions:

- $T2$ values obtained from individual fitting are two or three times higher for sample 8 (oil) than from simultaneous fitting
- the oil sample does not follow the model - the signal does not decay with increasing echo number - using individual $T2$ fitting
- the best quality series, regarding the deviation values, are:
  - for individual $T1$ fitting: the shortest $TE$ series
  - for individual $T2$ fitting: the longest $TR$ series
- simultaneous fitting is more precise, the parameters are fitted with smaller deviations

# Results - phantom

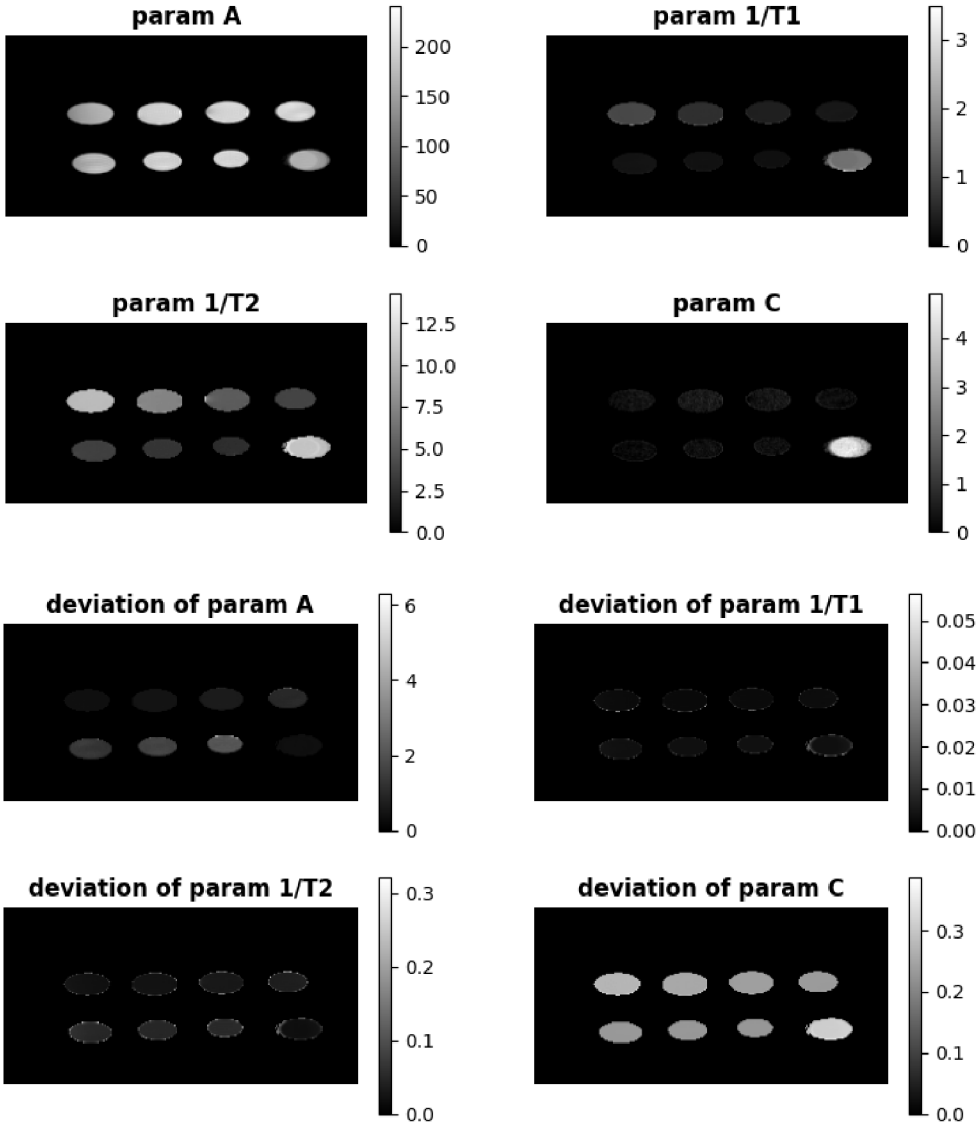


Fig. 5.11: Simultaneous fitting - phantom, all fitted parameters.

## Discussion - fixed rat brain

The fixed rat brain images, shown in Fig. 5.12, 5.13 and 5.14, display two distinct regions: the brain and the surrounding homogeneous agar gel. Although the gel itself is not the object of interest, homogeneity of the fitted parametric maps in this area is a co-indicator of the fitting quality. The results demonstrate several facts that may be important in applications:

- despite the inhomogeneous detection sensitivity, the quantitative maps of $R1$ and $R2$ are homogeneous in the whole brain, and the gel indicates reliability even in very dark areas. This can
  - facilitate brain segmentation: in the brain images, to highlight structures
  - be used to quantitation of contrast agent concentration
- the Gibbs artifact, resulting from limited k-space extent (i.e., limited spatial resolution), is manifested also in parametric maps, and may interfere with layered structures in the brain. For high quality imaging, data acquisition and image reconstruction should be designed to avoid this artifact
- corpus callosum is a typical white matter that appears dark on $A$. This corresponds to the water content: the average gray matter content is known to be 82%, white matter 68%. The estimated ratio is about 1.4, the expected is 1.2. Less water in white matter probably corresponds to the fact that there are nerve fibers and the space is probably more solid than in gray matter. In addition to the fact that there is less free water, the water relaxes faster, so $R1$ and $R2$ are higher than in gray matter. Due to the fixation of the brain with paraformaldehyde, which dehydrates the brain structures, the relaxation times were shortened
  - live brain $T1$ values [21] - gray matter 2000 ms, white matter 1700 ms
  - fixed brain $T1$ values - gray matter 800 ms, white matter 600 ms
  - live brain $T2$ values [21] - gray matter 38 ms, white matter 33 ms
  - fixed brain $T2$ values - gray matter 43 ms, white matter 29 ms
- outliers often occur at sharp edges

# Results - fixed rat brain

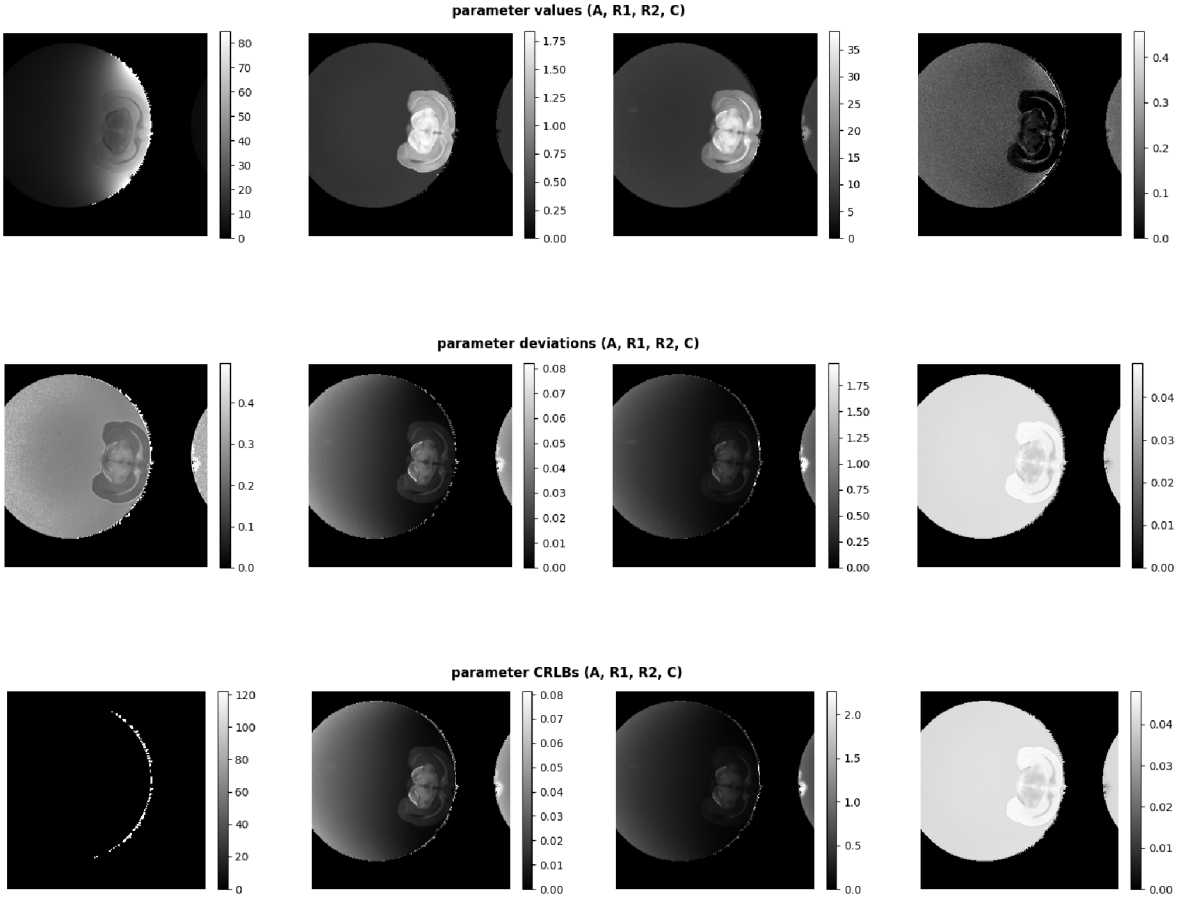


Fig. 5.12: Simultaneous fitting - fixed rat brain, whole FOV.

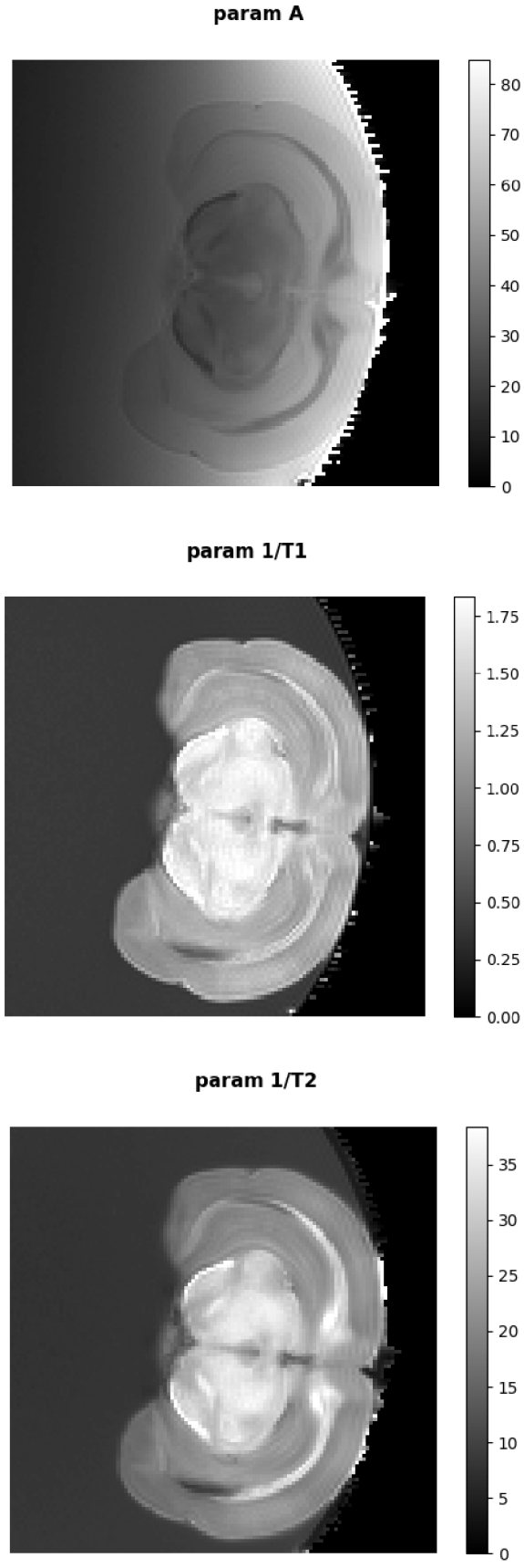


Fig. 5.13: Simultaneous fitting - fixed rat brain, zoomed.

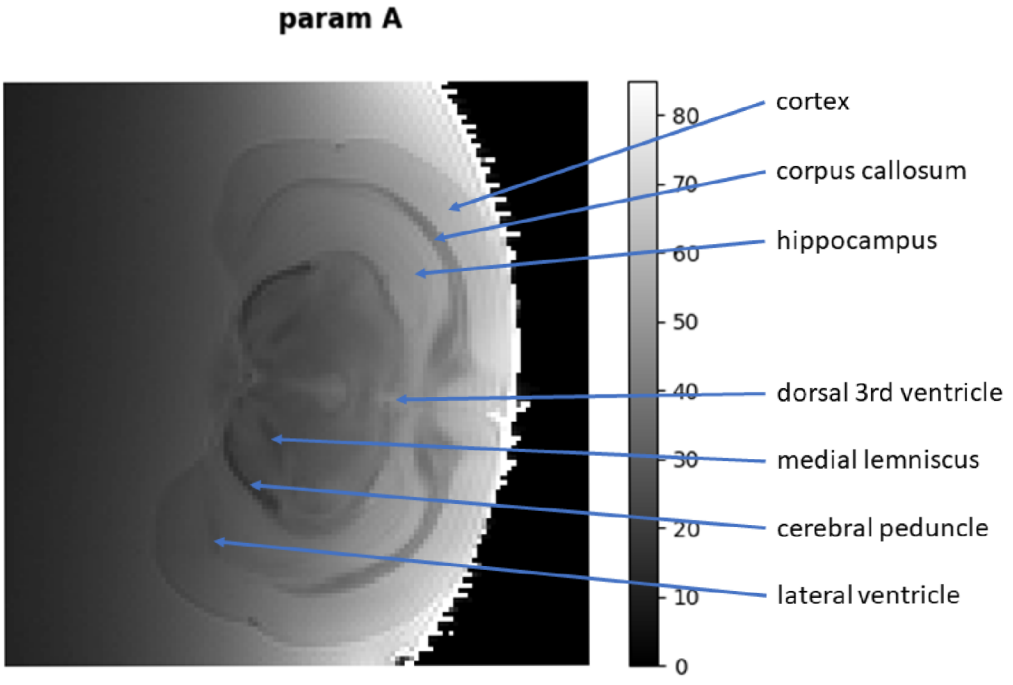


Fig. 5.14: Fixed rat brain anatomy.

# Resume

The aim of this bachelor's thesis was to implement the algorithm in Python for data analysis for quantitative MR relaxometry. The results were verified using data measured by preclinical Bruker Biospec 9.4 T scanner at ÚPT AV ČR, v. v. i.

At the beginning, the theoretical foundations were given in Chapter One, which focuses on MR theory and basic terms explanation. History of relaxation measurements from spectroscopy to state-of-the-art methods such as fingerprinting or deep learning is presented in Chapter Two. The Third Chapter discuss reasons for relaxometry.

The Fourth Chapter is finally dedicated to the algorithm implementation. There are described the methods used in the algorithm implementation and materials used to verify the results. In the Fifth Chapter, the results are presented and discussed.

Once the algorithm was designed, the phantom was measured and data were fitted. It was found that in the context of the data processed in this study, both approaches to precision assessment lead to the same result. Numerically the simpler linearized-neighborhood approach was found to be more stable.

The phantom contained Gd-nanoliposomes in different concentrations and control samples such as physiological saline or vegetable oil. The results are as expected, except for the oil sample. Finally the results were successfully verified on a relaxometry of a rat brain fixed in agar gel.

# Bibliography


[1] ABRAGAM, Anatole. *The principles of nuclear magnetism*. Reprinted. Oxford: Oxford University Press, 2011. The international series of monographs on physics. ISBN 978-0-19-852014-6.

[2] BERNSTEIN, Matt A., Kevin Franklin KING a Xiaohong Joe ZHOU. *Handbook of MRI pulse sequences*. Amsterdam: Academic Press, © 2004. ISBN 978-0-12-092861-3.

[3] BLOCH, F. Nuclear Induction. *Physical Review* [online]. 1946, **70**(7-8), 460-474 [cit. 2022-04-04]. ISSN 0031-899X. Available at: doi:10.1103/PhysRev.70.460

[4] BUXTON, Richard B. *Introduction to functional magnetic resonance imaging: principles and techniques*. Cambridge: Cambridge University Press, 2002. ISBN 0-521-58113-3.

[5] CARNEIRO, A. A. O., G. R. VILELA, D. B. de ARAUJO a O. BAFFA. MRI relaxometry: methods and applications. *Brazilian Journal of Physics* [online]. 2006, **36**(1a) [cit. 2021-11-10]. ISSN 0103-9733. Available at: doi:10.1590/S0103-97332006000100005

[6] CAVASSILA, S, S DEVAL, C HUEGEN, D VAN ORMONDT a D GRAVERON-DEMILLY. Cramér-Rao Bound Expressions for Parametric Estimation of Overlapping Peaks: Influence of Prior Knowledge. *Journal of Magnetic Resonance* [online]. 2000, **143**(2), 311-320 [cit. 2022-02-18]. ISSN 10907807. Dostupné z: doi:10.1006/jmre.1999.2002

[7] CAVASSILA, S., S. DEVAL, C. HUEGEN, D. VAN ORMONDT a D. GRAVERON-DEMILLY. Cramér-Rao bounds: an evaluation tool for quantitation. *NMR in Biomedicine* [online]. 2001, **14**(4), 278-283 [cit. 2022-02-18]. ISSN 09523480. Dostupné z: doi:10.1002/nbm.701

[8] CHANG, ALFRED E., YVEDT L. MATORY, ANDREW J. DWYER, et al. Magnetic Resonance Imaging Versus Computed Tomography in the Evaluation of Soft Tissue Tumors of the Extremities. *Annals of Surgery* [online]. 1987, **205**(4), 340-348 [cit. 2021-11-10]. ISSN 0003-4932. Available at: doi:10.1097/00000658-198704000-00002

[9] CHEN, Yong, Zhenghan FANG, Sheng-Che HUNG, Wei-Tang CHANG, Dinggang SHEN a Weili LIN. High-resolution 3D MR Fingerprinting using parallel imaging and deep learning. *NeuroImage* [online]. 2020, **206** [cit. 2021-11-09]. ISSN 10538119. Available at: doi:10.1016/j.neuroimage.2019.116329

[10] COUSINS, J P. Clinical MR spectroscopy: fundamentals, current applications, and future potential. *American Journal of Roentgenology* [online]. 1995, **164**(6), 1337-1347 [cit. 2022-01-01]. ISSN 0361-803X. Avilable at: doi:10.2214/ajr.164.6.7754871

[11] DAMADIAN, Raymond. Tumor Detection by Nuclear Magnetic Resonance. *Science* [online]. 1971, **171**(3976), 1151-1153 [cit. 2021-12-03]. ISSN 0036-8075. Available at: doi:10.1126/science.171.3976.1151

[12] DEONI, Sean C.L. Quantitative Relaxometry of the Brain. *Topics in Magnetic Resonance Imaging* [online]. 2010, **21**(2), 101-113 [cit. 2021-10-30]. ISSN 0899-3459. Available at: doi:10.1097/RMR.0b013e31821e56d8

[13] FENG, Li, Dan MA a Fang LIU. Rapid MR relaxometry using deep learning: An overview of current techniques and emerging trends. *NMR in Biomedicine* [online]. [cit. 2021-11-09]. ISSN 0952-3480. Available at: doi:10.1002/nbm.4416

[14] GRANZIERA, Cristina, Jens WUERFEL, Frederik BARKHOF, et al. Quantitative magnetic resonance imaging towards clinical application in multiple sclerosis. *Brain* [online]. 2021, **144**(5), 1296-1311 [cit. 2021-10-30]. ISSN 0006-8950. Available at: doi:10.1093/brain/awab029

[15] HAHN, E. L. Spin Echoes. *Physical Review* [online]. 1950, **80**(4), 580-594 [cit. 2021-11-26]. ISSN 0031-899X. Available at: doi:10.1103/PhysRev.80.580

[16] HAMILTON, Jesse I. a Nicole SEIBERLICH. Machine Learning for Rapid Magnetic Resonance Fingerprinting Tissue Property Quantification. *Proceedings of the IEEE* [online]. 2020, **108**(1), 69-85 [cit. 2021-11-09]. ISSN 0018-9219. Available at: doi:10.1109/JPROC.2019.2936998

[17] HSIEH, Jean J. L. a Imants SVALBE. Magnetic resonance fingerprinting: from evolution to clinical applications. *Journal of Medical Radiation Sciences* [online]. 2020, **67**(4), 333-344 [cit. 2021-11-09]. ISSN 2051-3895. Available at: doi:10.1002/jmrs.413

[18] JOHANSEN-BERG, Heidi a Timothy E. J. BEHRENS. *Diffusion MRI: from quantitative measurement to in-vivo neuroanatomy*. Amsterdam: Elsevier/Academic Press, 2009. ISBN 978-0-12-374709-9.

[19] KEENAN, Kathryn E., Maureen AINSLIE, Alex J. BARKER, et al. Quantitative magnetic resonance imaging phantoms: A review and the need for a system phantom. *Magnetic Resonance in Medicine* [online]. 2018, **79**(1), 48-61 [cit. 2021-11-25]. ISSN 07403194. Available at: doi:10.1002/mrm.26982

[20] KRAFT, K. A., P. P. FATOUROS, G. D. CLARKE a P. R. S. KISHORE. An MRI phantom material for quantitative relaxometry. *Magnetic Resonance in Medicine* [online]. 1987, **5**(6), 555-562 [cit. 2021-10-30]. ISSN 07403194. Available at: doi:10.1002/mrm.1910050606

[21] KUO, Yu-Ting, Amy H. HERLIHY, Po-Wah SO, Kishore K. BHAKOO a Jimmy D. BELL. In vivo measurements of T1 relaxation times in mouse brain associated with different modes of systemic administration of manganese chloride. *Journal of Magnetic Resonance Imaging* [online]. 2005, **21**(4), 334-339 [cit. 2022-05-27]. ISSN 1053-1807. Available at: doi:10.1002/jmri.20285

[22] LIBERMAN, Gilad, Yoram LOUZOUN a Dafna BEN BASHAT. T 1 Mapping using variable flip angle SPGR data with flip angle correction. *Journal of Magnetic Resonance Imaging* [online]. 2014, **40**(1), 171-180 [cit. 2021-11-25]. ISSN 10531807. Available at: doi:10.1002/jmri.24373

[23] MARGARET CHENG, Hai-Ling, Nikola STIKOV, Nilesh R. GHUGRE a Graham A. WRIGHT. Practical medical applications of quantitative MR relaxometry. *Journal of Magnetic Resonance Imaging* [online]. 2012, **36**(4), 805-824 [cit. 2021-11-10]. ISSN 10531807. Available at: doi:10.1002/jmri.23718

[24] MILFORD, David, Nicolas ROSBACH, Martin BENDSZUS, Sabine HEILAND a Xiaobing FAN. Mono-Exponential Fitting in T2-Relaxometry: Relevance of Offset and First Echo. *PLOS ONE* [online]. 2015, **10**(12) [cit. 2021-11-25]. ISSN 1932-6203. Available at: doi:10.1371/journal.pone.0145255

[25] ROBERTS, John D. The Bloch equations. How to have fun calculating what happens in NMR experiments with a personal computer. *Concepts in Magnetic Resonance* [online]. 1991, **3**(1), 27-45 [cit. 2021-12-01]. ISSN 10437347. Available at: doi:10.1002/cmr.1820030104

[26] WAHSNER, Jessica, Eric M. GALE, Aurora RODRÍGUEZ-RODRÍGUEZ a Peter CARAVAN. Chemistry of MRI Contrast Agents: Current Challenges and New Frontiers. *Chemical Reviews* [online]. 2019, **119**(2), 957-1057 [cit. 2021-11-09]. ISSN 0009-2665. Available at: doi:10.1021/acs.chemrev.8b00363

[27] XIAO, Yu-Dong, Ramchandra PAUDEL, Jun LIU, Cong MA, Zi-Shu ZHANG a Shun-Ke ZHOU. MRI contrast agents: Classification and application (Review). *International Journal of Molecular Medicine* [online]. 2016, **38**(5), 1319-1326 [cit. 2021-11-09]. ISSN 1107-3756. Available at: doi:10.3892/ijmm.2016.2744

[28] YOUNG, Ian. Nuclear magnetic resonance imaging. *Electronics and Power* [online]. 1984, **30**(3), 205-210 [cit. 2021-11-25]. ISSN 00135127. Available at: doi:10.1049/ep.1984.0112

# Symbols and abbreviations

| | |
|---|---|
| **2DFT** | 2D Fourier transform |
| **BBB** | Blood brain barrier |
| **CT** | Computed tomography |
| **DIR** | Double inversion recovery |
| **ECF** | Extracellular fluid |
| **EPI** | Echo planar imaging |
| **ESP** | Echo spacing |
| **ETL** | Echo train length |
| **FA** | Flip angle |
| **FFE** | Fast field echo |
| **FFT** | Fast Fourier transform |
| **FID** | Free induction decay |
| **FISP** | Fast imaging with steady (-state free) precession |
| **FLAIR** | Fluid attenuated inversion recovery |
| **FLASH** | Fast low-angle shot |
| **FOV** | Field of view |
| **FSE** | Fast spin echo |
| **GBCAs** | Gadolinium based contrast agents |
| **Gd** | Gadolinium |
| **Gd-DTPA** | Gadolinium (III) diethylenetriamine pentaacetate |
| **GI** | Gastrointestinal |
| **GRASE** | Gradient and spin echo |
| **GRASS** | Gradient recalled acquisition in the steady state |
| **GRE** | Gradient echo |

| | |
|---|---|
| **IFT** | Inverse Fourier transform |
| **IR** | Inversion recovery |
| **MR** | Magnetic resonance |
| **MRF** | Magnetic resonance fingerprinting |
| **MRI** | Magnetic resonance imaging |
| **MSE** | Multi spin echo |
| **NMR** | Nuclear magnetic resonance |
| **PET** | Positron emission tomography |
| **RARE** | Rapid acquisition with relaxation enhancement |
| **RF** | Radiofrequency |
| **SE** | Spin echo |
| **SNR** | Signal-to-noise ratio |
| **SPGR** | Spoiled gradient echo |
| **SPIOs** | Superparamagnetic iron oxides |
| **SR** | Saturation recovery |
| **SSFP** | Steady state free precession |
| **STIR** | Short time inversion recovery |
| **T1** | T1 relaxation time |
| **T1-FFE** | T1 fast field echo |
| **T2** | T2 relaxation time |
| **T2*** | T2* relaxation time |
| **TE** | Echo time |
| **TGSE** | Turbo gradient spin echo |
| **TIR** | Triple inversion recovery |
| **TR** | Repetition time |

# A Contents of the electronic attachment

The electronic attachment contains all the Python scripts and a file with the image results of fitting.

```
/ ..... the root directory of the attached archive
├── images.pdf ..... image attachments
└── codes ..... Python scripts
    ├── individual_T1_fitting.py
    ├── individual_T2_fitting.py
    └── simultaneous_fitting.py
```